Spectroscopy of Charge Carriers at Ionic Liquid/Semiconductor Interfaces

Timothy Luke Atallah

Submitted in partial fulfillment of the
requirements for the degree of
Doctor of Philosophy
under the Executive Committee
of the Graduate School of Arts and Science

COLUMBIA UNIVERSITY

2017

ABSTRACT

Spectroscopy of Charge Carriers at Ionic Liquid/Semiconductor Interfaces

Timothy Luke Atallah

The interface of semiconductors plays an important role in all semiconductor devices - often defining the device's properties. Ionic liquids are typically employed as gating dielectrics to achieve high charge densities at semiconductor surfaces. Such ionic liquid/semiconductor interfaces are usually studied using electrical transport techniques, which often have the drawback of requiring modeling to achieve an understanding of the species involved in the devices at the ionic liquid/semiconductor interfaces. Through the use of infra-red and optical spectroscopy this work seeks to uncover the nature of charge carriers surface of both organic semiconductors, specifically rubrene, and two dimensional semiconductors, specifically mono-layer MoS_2, and how these charges interact in the presence of mobile ions. I show that for rubrene infra-red spectroscopy reveals with the formation of an ionic liquid/rubrene interface the rubrene surface becomes intrinsically hole doped. Additionally, that when rubrene is gated the ionic liquid to achieve high charge densities in rubrene there is a saturation of the conductive species resulting in a lowering of hole mobility. In the case of monolayer MoS_2 photoluminescence spectroscopy shows that forming the ionic liquid/MoS_2 interface results in mobile ions screen the charged defects in the MoS_2 increasing the photoluminescence intensity.

Contents

List of Figures

Acknowledgements

Nam dui ligula, fringilla a, euismod sodales, sollicitudin vel, wisi. Morbi auctor lorem non justo. Nam lacus libero, pretium at, lobortis vitae, ultricies et, tellus. Donec aliquet, tortor sed accumsan bibendum, erat ligula aliquet magna, vitae ornare odio metus a mi. Morbi ac orci et nisl hendrerit mollis. Suspendisse ut massa. Cras nec ante. Pellentesque a nulla. Cum sociis natoque penatibus et magnis dis parturient montes, nascetur ridiculus mus. Aliquam tincidunt urna. Nulla ullamcorper vestibulum turpis. Pellentesque cursus luctus mauris.

There are so many who need to be acknowledged and thanked for helping get this ordeal we call a PhD. Indeed, so many have to suffer with me and bear with me because of my flaws. However, despite all the trials (not least was the frustration of moving from Texas to New York) they have helped me to grow as a scientist and perhaps more importantly as a person.

To begin, I would like to thank all those who I got to know in Texas who remained behind, who were friends to me in a new place. In particular I would like to mention Dr. Joshua Morris with whom I started by PhD career in Texas who started to show me the ropes of the XYZ lab and was a dear friend who introduced me to drinking coffee, going to Longhorn football games and invited me over to hang out and play Starcraft on weekends.

Next I would like to thank all those who moved from Texas to New York, who had to go through the ordeal of moving twice. Perhaps, most debilitating was the atmosphere of constant frustration due to delays and failing to achieve results even the presence of overwhelming pressure. Yet through it all we stood together and would eat and drink together - to the point that our group lunches became legendary. We supported one another through the most depressing times and finally emerged - stronger and more persevering. In particular, I would like to mention Dr. Kristopher Wayne Williams whom joined the XYZ lab with me in Texas and stuck through it all and was by my side through the thick and the thin. Always a friend and supportive and never negative or hostile: an anchor whom I could

rely on who had my back!

Since I have been at Columbia so many phenomenal people have joined the XYZ lab. People whom I have shared a lab and beer with. Whom I have poured my difficulties into and heard theirs. It has been amazing working along side, helping and being helped by them. I would like especially to mention Dr. Martin Gustafsson who was extremely supportive during my hardest moments who never gave up confidence in me and was willing to give so much time and effort to help me to succeed. Other great mentors I would mention are "Herr" Dr. Daniel Niesner, Dr. Tuan Trinh, Dr. Fang Liu and Dr. Kiyoshi Miyata whom have been mentors and great scientists to bounce ideas around with. I need to mention all the junior graduate students whom have made graduate school at Columbia such a great experience especially Tyler Evans (aka Tynie), Bryan Kudisch (aka Bynie), Jue Wang, Felisa Conrad-Burton (aka Felisi), Michael Spencer, Drew Schlaus (aka Drewcifer) (and Koba), Kihong Lee (aka KiLee), Xinjue Zhong, Prakriti Joshi. Also, all the high school and undergraduate students I mentored: Paul Kleiman, Monica Theibault and Melissa Bosch.

The Columbia community was so welcoming when I arrived from Texas and I want to thank them for being so hospitable and friendly and accepting and supportive. I want to mention the Campos lab that put up with me on their office space, especially Dr. Helen Tran who was a friend from the beginning. Also Dr. Yu Zhong and Dongje Seo who were so helpful whenever I needed something related to sample preperation. Special thanks to Dr. Colin Nuckolls, Dr. James Hone and Dr. Louis Brus who let me make use of their lab space and equipment for many of my measurements. Additionally, I would like to thank Dr. Ann McDermott who let me TA with her and was such an amazing mentor and support when it came to teaching. All the professor I have met at Columbia have been so supportive and helpful despite having busy schedules.

Away from Columbia I would like to thank Dr. Vitaly Podzorov and Dr. Yuanzhen Chen at Rutgers without whom I don't think I would have managed the rubrene project. Also Dr.

even though he was in Portugal - he was willing to give me advice with the graduate school experience and life and how to look at the brighter future!

Most recently, my girlfriend, Carman Chan, has been an encouragement pushing and supporting me through this last stretch before the end; even though I was getting frustrated and want to give up. Thank you, Carmen!

Finally, but perhaps most importantly, I would like thank my God and savior Jesus Christ. My graduate school experience has been far from smooth sailing, but in it all I have learned to lean on Jesus (at times more than others). But through it all I felt Him by me and I thank him for the lessons learned and growth he has enabled me to do. I feel so very blessed by the people he has led me to meet and faith he has instilled in me.

Dedication

My work and thesis are dedicated to my nephew, Kai Niko Atallah, and my god-daughter, Adela Charlotte Stahl. They have been stars in my life these last few years: full of life and curiosity; reminding of why I went into science.

Chapter 1

Charges at Semiconductor Interfaces

1.1 Introduction

Understanding semiconductor interfaces lies at the heart of explaining almost all modern electronic devices. In particular, for a field effect transistor (FET) the interface between a semiconductor and gating dielectric can govern the overall device electrical transport properties as the dielectric material (or lack thereof) may modify how charges move in the semiconductor. In this thesis I present my work in understanding two different questions that arise in two distinct semiconductor interfaces respectively:

1. **Why is there a negative transconductance for the transport of holes in a rubrene/ionic liquid (IL) gated FETs?**

2. **Can we understand and mitigate charge-defect scattering in monolayer MoS_2 using ILs?**

1.2 Charge Transport at the Surface of Rubrene

1.2.1 Introduction to Organic Semiconductors for FETs

Over the past decades significant interest has existed in developing organic semiconductors for technological applications. Organic semiconductors are potentially lucrative since they typically require lower temperature processing (including printable),[1] making them a much more economical material than conventional inorganic semiconductors like Si for device fabrication and they are highly functionalizable: organic chemists are capable of appending a variety of functional groups to the organic semiconductor molecules potentially tuning their structural and electronic properties for niche applications.

However, years of research and development on these semiconductors have shown that the advantages of organic semiconductors come with severe drawbacks: devices typically are much less efficient to be competitive with their well established conventional Si or GaAs
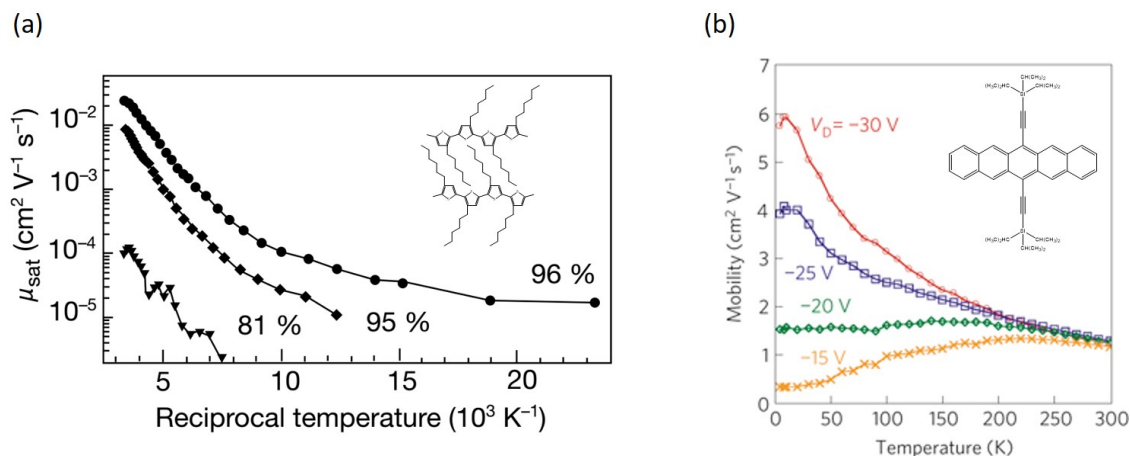
Figure 1.1: (a) A plot of the hole mobility, μ, as function of reciprocal temperature, $\frac{1}{T}$, of an organic polymer, p3HT, popularly used in FETs and photovoltaics (the percentages correspond to how well packed the polymer is on the film). At lower $\frac{1}{T}$ (or higher T) the mobility is higher, indicating a slow thermally-activated mobility. Reprinted by permission from Macmillan Publishers Ltd: Nature, reference 2, copyright 1999. (b) A plot of the hole mobility as function of temperature for TIPS-Pentacene, an oligoacene derivative. With high enough driving voltage, V_D, the mobility increases as temperature is lowered suggesting a bandlike transport mechanism. Reprinted by permission from Macmillan Publishers Ltd: Nature Materials, reference 3, copyright 2010.

rivals. This is largely due to the disorder in solution processed organic semiconductor films resulting in small crystalline domains with many domain boundaries limiting charge transport (this is particularly true for polymers[2]) and the strong electron-phonon coupling resulting in self-trapped charges (i.e. small polarons[4] and Frenkel excitons) which require thermal activation for transport (figure 1.1 (a)) limiting the electron/hole/exciton mobilities in such materials. Furthermore, organic semiconductors at their interface are more vulnerable to oxidative stresses (unlike Si which grows a native oxide to protect from more damage): this further hampers their charge transport capabilities by introducing deeper traps for charges to get stuck in.[5]

Fortunately, one class of organic semiconductors that emerged as a champion in producing high mobility FETs: the oligacenes. In particular pentacene[3] and rubrene[6] (a tetracene derivative) proved to have hole mobilities rivaling that of amorphous Si, band-like transport (i.e. thermally *deactivated* mobilities shown in figure 1.1 (b)) and some resistance to developing surface defects. Rubrene in particular is of interest due to the ease of synthesis, ease of sizable crystal growth and robustness against oxidation.[7]

1.2.2 Rubrene

Taking a closer look at rubrene: the transport properties are dominated by the electronic bands made up of π orbitals. The π being the highest occupied molecular orbital (HOMO) which hybridizes into the valence band (VB) and the π^* the lowest unoccupied molecular orbital (LUMO) which hybridizes into the conduction band (CB). The Van der Waals crystal packing structure for rubrene forms a herringbone geometry with rubrene's tetracene backbone (Figure 1.2) in the crystal's a and b directions meaning the intramolecular $\pi - \pi$ stacking are dominantly along these axes.[8] Hence, the crystal growth is more favorable along these axes. This is also convenient since the $\pi - \pi$ stacking results in favorable charge delocalization along these axes. Therefore, a and b crystalline axes have the

3
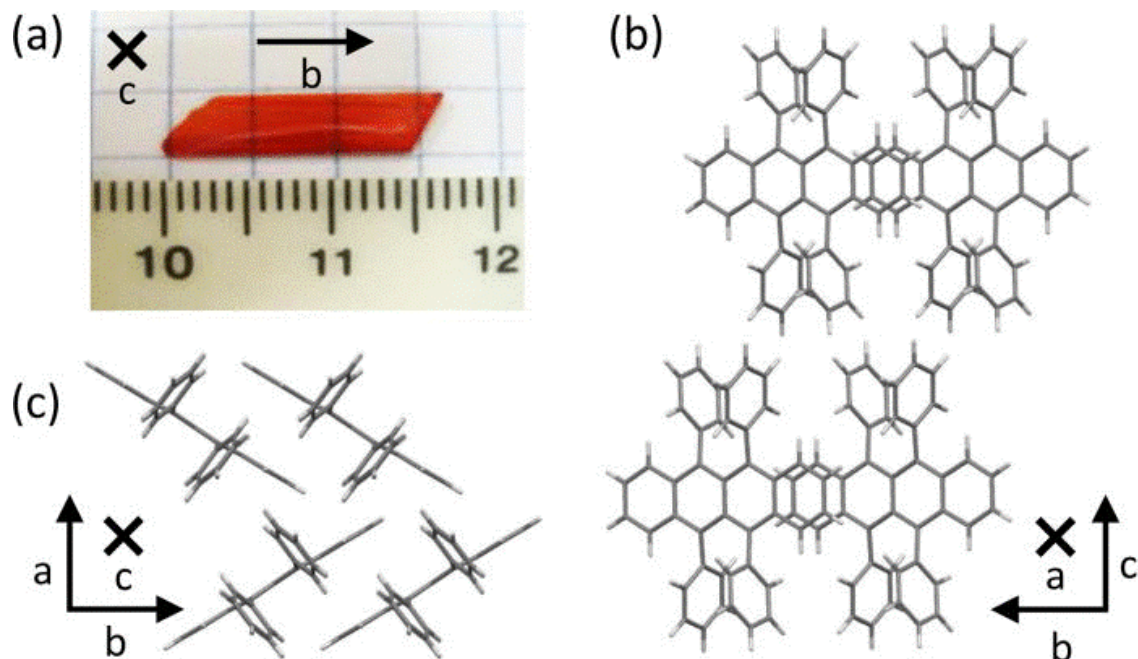
Figure 1.2: (a) Centimeter sized rubrene crystal with a ruler for reference. (b) Rubrene crystalline stacking as viewed down the a axis, the b can be seen as how the oligoacene backbone allowing for intramolecular $\pi - \pi$ orbital stacking indicating favorable delocalization of the electronic wavefunction along that axis. (c) Rubrene crystalline stacking as viewed down the c axis showing the herringbone geometry. Both the a and b show $\pi - \pi$ orbital stacking explaining the high mobility in those directions. Reprinted from 9, with the permission of AIP Publishing.

highest hole mobilities. Large crystals along the a and b directions makes fabricating efficient FETs relatively straightforward not requiring any costly lithographic techniques.[6]

Rubrene Crystal Growth by Physical Vapor Transport

The rubrene source material was purchased from a vendor. Rubrene crystals were grown by horizontal physical vapor transport. Thick (> 10 μm in thickness) crystals with single-crystalline surfaces (seen as highly reflective with no visual defects under optical microscopy) were selected for subsequent device fabrication. For good quality crystals, the maximum temperature in the furnace was $T_{max} \sim 310$ °C and flow rate of N_2 carrier gas $f_{N_2} = 100$ mL·min^{-1}; for poor quality crystals, $T_{max} \sim 350$ °C, $f_{N_2} > 100$ mL·min^{-1}.[10]

1.2.3   Rubrene Field Effect Transistors

Metal-Insulator-Semiconductors Capacitors

Since rubrene grows large (~ 1 cm^2 as seen in figure 1.2 (a)) and high purity crystals, macroscopic single crystal FET fabrication is straightforward. These FETs can then be used to study the intrinsic electrical transport at the surface of the crystal (or rather at the rubrene/dielectric interface). FETs can be thought of being made of metal-insulator(dielectric)-semiconductor (MIS) capacitor and an additional electrode. Once the semiconductor/dielectric interface (called the "channel") is charged, current can flow through the surface of a semiconductor behaving like a (ideally, neglecting any many-body effects) metal.[11] By applying a gating voltage, V_G, across the insulator the semiconductor's band alignment shifts to place the Fermi energy, E_F, either in the conduction band (CB), resulting in electron doping or valence band (VB) resulting in hole doping. This is schematically shown in figure 1.3.

Practically, this charge injection follows the standard capacitance equation:

$$\frac{\partial q}{\partial A} = \frac{\partial C}{\partial A} \left(V_G - V_T \right) \tag{1.1}$$

where, q, corresponds to the amount of charge injected, A, the area of the insulator/ semiconductor interface, C, the capacitance as defined by the dielectric and geometry, V_G, the applied gate voltage across the MIS and V_T the threshold voltage corresponding to the energy required to shift the E_F out of the semiconductor gap.*
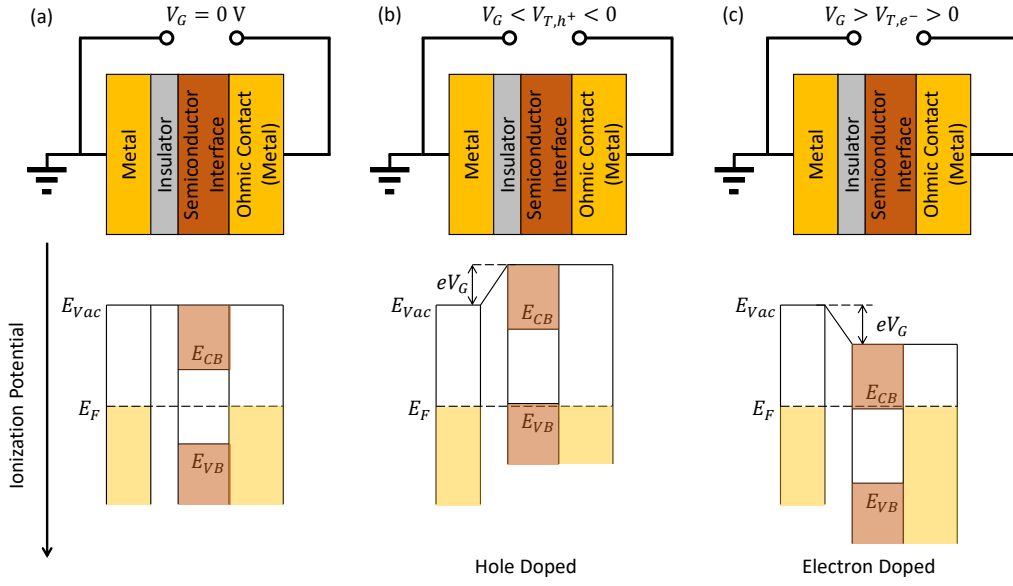
Figure 1.3: A simplified MIS capacitor geometry (top) with an energy level diagram (bottom) corresponding to the scenario in the geometry above with different applied gate voltages, V_G. (a) $V_G = 0$ V so the E_F is in the semiconductor gap. (b) $V_G < 0$ V such that there is an electric field across the insulator and the semiconductor vacuum energy, E_{Vac}, as been raised by eV_G (e is the fundamental electric charge) and now $E_F < E_{CB}$ so holes have been injected into the semiconductor's interface. (c) Now $V_G > 0$ V and the semiconductor vacuum energy, E_{Vac}, as been lowered by eV_G (e is the fundamental electric charge) and now $E_F > E_{CB}$ so electrons have been injected into the semiconductor's interface.

Field Effect Transistors

Adding one more electrode (typically called a drain) to the device turns a MIS into FET as illustrated in figure 1.4. Now applying a gate voltage, V_G, charges the semiconductor interface giving a surface charge density, $\frac{\partial q}{\partial A}$, as defined above in the MIS by equation 1.1. Then applying bias across the source and drain, V_{SD} that accumulated charge density flows at the dielectric/semiconductor interface as a current, I_{SD}. Hence, semiconductor/dielectric interface or channel, behaves effectively like a simple resistor following Ohm's law:[12]

$$I_{SD} = \left(\frac{1}{R}\right) V_{SD} = \left(\frac{1}{\rho_\square} \frac{W}{L}\right) V_{SD} = (G) V_{SD} = \left(g_\square \frac{W}{L}\right) V_{SD} \tag{1.2}$$

---

*In the idealized MIS shown in figure 1.3 gives $V_T = \frac{|E_{VB} - E_{CB}|}{2e}$. Typically, due to the presence of sub-gap defect states, imperfect metal/semiconductor or semiconductor/dielectric interfaces, Schottky barriers, etc... practically this relation rarely holds true.
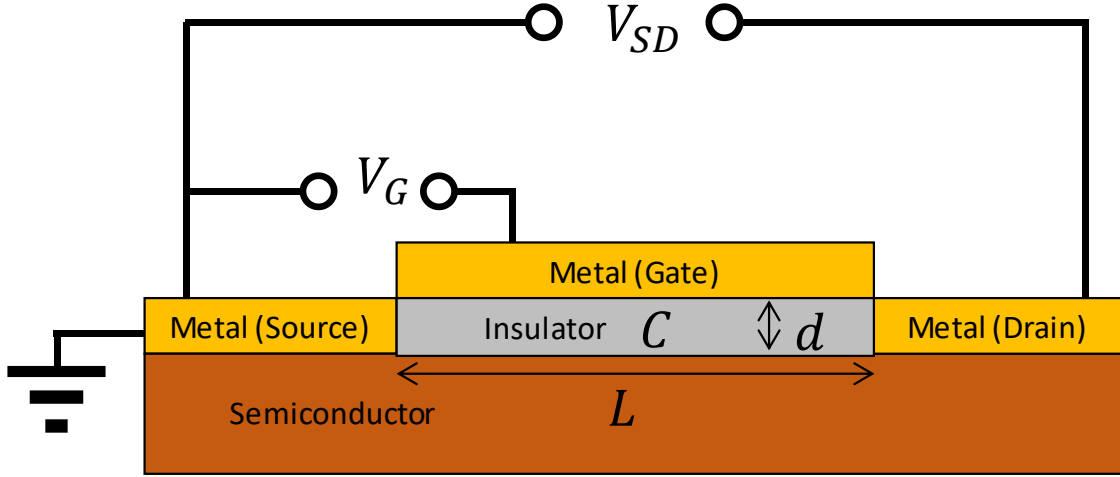
Figure 1.4: A schematic of an FET showing a semiconductor with a channel length, L, gated with an insulator with capacitance, C and thickness, d. The charge density in the channel is given by equation 1.1, which relies on applying a voltage, V_G, across the gate and source electrode. Current flows through the semiconductor channel at the semiconductor/dielectric interface when a voltage, V_{SD}, is applied across the source and drain electrodes.

with R (G) being the resistance (conductance) of the channel. $\rho_\square$ ($g_\square$) correspond to the sheet resistivity (conductivity) and the $\frac{W}{L}$ the ratio of the channel length, L, to width, W. We can show that $g_\square$ depends on the amount of charge in the channel, $\frac{\partial C}{\partial A}(V_G - V_T)$, and how fast the charge moves in the channel given an applied electric field, μ, or mobility such that:[13]

$$I_{SD} = \mu \left(\frac{\partial C}{\partial A}\right) \left(\frac{L}{W}\right) (V_G - V_T) V_{SD} \tag{1.3}$$

Hence, there is a linear transfer (i.e. I_{SD} vs V_G) and output relationship (i.e. I_{SD} vs V_{SD}) as seen in figure 1.5(b). Note that this only holds true if we have a uniform charge density across our semiconductor/dielectric interface. This requires:

$$|V_{SD}| << (V_G - V_T) \tag{1.4}$$

If this does not hold true, then the charge density in the channel may deplete faster than it can be recovered by the gating voltage, eventually achieving a saturation regime. This results in different transfer and output characteristics and equation 1.3 is no longer applicable.[11] We will focus on measurements within the linear regime.

Charge-Carrier Mobility, μ

Equation 1.3 gives a transconductance:

$$g_m = \frac{\partial I_{SD}}{\partial V_G} = \mu \left(\frac{\partial C}{\partial A} \right) \left(\frac{L}{W} \right) V_{SD} \tag{1.5}$$

from which we can extract the much sought after, μ, i.e. the ratio drift velocity of a charge, v, to the applied electric field, $|\mathbf{E}|$:

$$v = \mu \, |\mathbf{E}| \tag{1.6}$$

at the semiconductor/dielectric interface. Semi-classically, μ represents the averaging of many physical processes as the charge travels through the semiconductor (at the interface):[14]

$$\mu = \frac{e}{m^*} \langle \tau \rangle \tag{1.7}$$

with e being the elemental charge, m^* the effective mass and $\langle \tau \rangle$ the average scattering time convolving scattering with/into/out-of traps, grain boundaries, interfacial defects, impurities, phonons, etc... For highly crystalline and pure conventional inorganic semiconductor materials like single crystalline Si, Ge, GaAs the effective mass is small (given by the curvature of the valence/conduction band, the effective charge mass, m^*, is less than the electron mass) and long scattering times (i.e. the charge does not run into phonons and defects often) the mobility is very high ($\mu\,(300\ \mathrm{K}) > 10^3\ \mathrm{cm^2 V^{-1} s^{-1}}$) producing faster and more efficient

electronic devices. Furthermore, reducing the material's temperature, T, reduces the probability of scattering with phonon modes, increasing τ_{ph}, (which typically is the limiting factor in pure and crystalline materials as effective mass is mostly temperature invariant) which results in an increase in mobility (i.e. $\frac{\partial \mu}{\partial T} < 0$); this is a hallmark for "bandlike" transport.[†] For most thin film organic semiconductors this is not the case: the electron/hole-phonon coupling is so strong that the charge distorts the lattice around it, self-trapping and localizing the charge into a (small) polaron.[4,15] This gives a very low mobility ($\mu < 0.1$ cm^{2}V^{-1}s^{-1}) as the m^* is very large since the charge is carrying the lattice distortion with it (equivalently the polaron dispersion curvature is very small) and the dominating form of charge drift is governed by phonon scattering resulting in ionization out of these self-traps which is thermally activated giving a $\frac{\partial \mu}{\partial T} > 0$.

Rubrene FET Mobilities

The situation becomes more interesting in the case of highly crystalline organic semiconductors, like rubrene. Being an organic semiconductor, the electron-phonon coupling is still very strong, however in the case of a pristine single crystal there is no scattering from impurities, defects and grain boundaries to localize the charge, hence the Bloch wave may exist for the electron density in rubrene. Indeed when using a air-gated single-crystal FET (hence any scattering from the dielectric/rubrene interface is suppressed and the properties are solely from the rubrene surface itself), the mobility is shown to be tens of cm^{2}V^{-1}s^{-1} and thermally deactivated, $\frac{\partial \mu}{\partial T} < 0$ as seen in figure 1.5 (c). These are clear signs of bandlike transport in the organic semiconductor making it ideal for studying to understand why rubrene possesses these properties for designing other viable organic semiconductors.

[†]**Bandlike** refers to electron/hole transport that behaves like a delocalized electron/hole within a material well described by an effective mass, m^*, without any many-body-effects and only scattering off of the lattice (phonons).
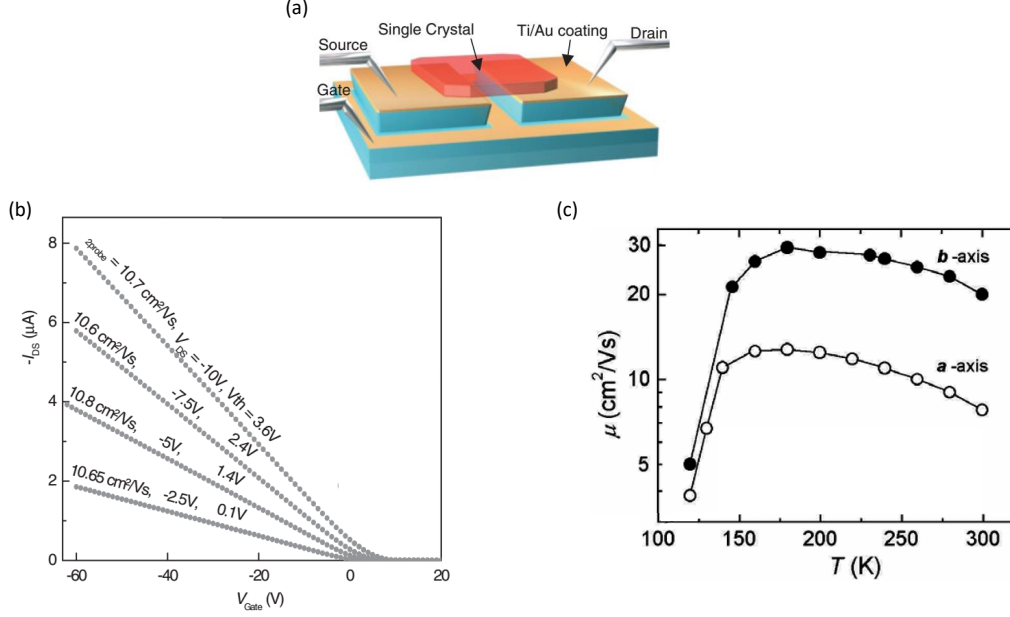
Figure 1.5: (a) An illustration of a air-gated single crystal rubrene FET made from a PDMS stamp. (b) Transfer curves from an air-gated single crystal rubrene FET, current through the channel, I_{SD} (also seen is I_{DS} or I_D), as function of gating voltage, V_G. The different curves correspond to different voltages across the source and drain, V_{SD}. The mobility, μ, derived from equation 1.3. Figures (a) and (b) reprinted from 16, with the permission of John Wiley and Sons Publishing. (c) Rubrene's mobility as function of temperature showing bandlike transport with $\frac{\partial \mu}{\partial T} < 0$ for $T > 160$ K. The different curves show the mobilities along the different axes of rubrene with $\pi - \pi$ stacking. Figure (c) adapted with permission from reference 7. Copyrighted by the American Physical Society.

1.2.4 Ionic Liquid Gating

However, another problem remains in organic FETs: the voltages required to turn on the FETs for viable commerical usage are too high (V_{SD} & $V_G > 5$ V) to achieve reasonable currents. One way to achieve a high current, I_{SD}, is with a high charge density, as shown by equation 1.3. To get a high charge density at low V_G a high capacitance, $\frac{\partial C}{\partial A}$, is required. If we consider the MIS part of the FET to be a parallel plate capacitor (which often gives a satisfying description of the system in most FETs) the equation for the capacitance is the following:

$$\frac{\partial C}{\partial A} = \varepsilon_0 \frac{\varepsilon_r}{d} \tag{1.8}$$

10

where ε_0 is the vacuum permittivity, ε_r is the relative permittivity and d the thickness of the dielectric. So to achieve a large capacitance one could use a dielectric with a larger ε_r or a smaller d. A typical way to get a very small d, is gating using an ionic liquid (IL) dielectric. An ionic liquid is an ionic compound (i.e. a salt) that is a liquid (i.e. molten) at room temperature. An example ionic liquid is shown in figure 1.6(a).
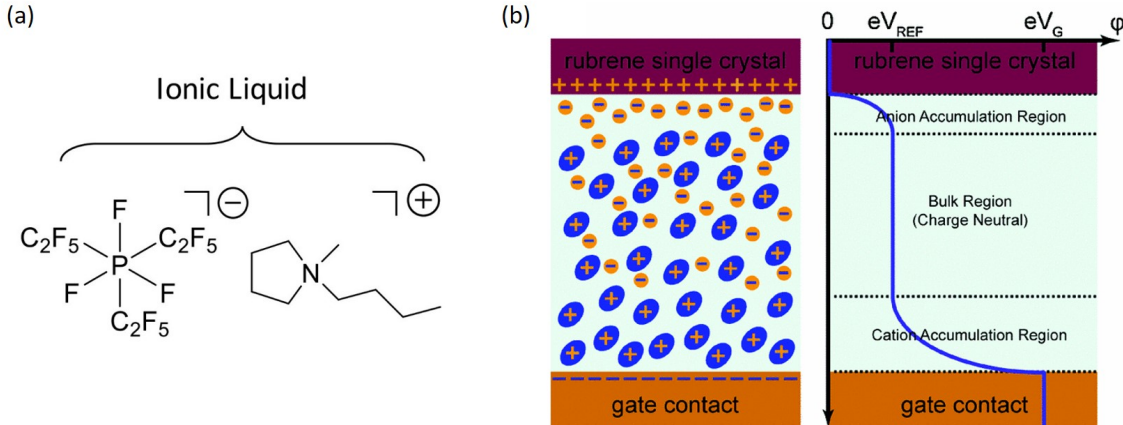
Figure 1.6: (a) An example of ionic liquid, [1-butyl-1-methyl pyrrolidinium][tris(pentafluoroethyl)trifluorophosphat] or [P14][FAP]. As with most ionic liquids it is made up of two greasy organic ions, making crystallization less favorable. A schematic diagram showing the electric double layer in a rubrene IL MIS capacitor geometry resulting in the hole injection at the rubrene surface. The right side figure illustrates the chemical potential energy (or electric potential) as function of location along the thickness of the MIS capacitor. Reprinted figure (b) with permission from 17: Yu Xia, Wei Xie, P. Paul Ruden, and C. Daniel Frisbie, Phys. Rev. Lett., 105, 036802, 2010. Copyright 2010 by the American Physical Society.

When a V_G is applied across an IL they form an electric double layer (EDL) with ions at the surface of the electrodes (metal or semiconductor) giving an effective $d_{EDL} \sim 1$ nm. The electric potential in an IL MIS structure as a result of a V_G is illustrated in figure 1.6(b) showing the voltage drop on the rubrene/anion interface from the EDL. This results in a capacitance on the order of $\frac{\partial C_{IL}}{\partial A} \sim 1$ $\mu F/\text{cm}^2$ (compare to 300 nm of SiO$_2$ gate dielectric which gives $\frac{\partial C_{\text{SiO}_2}}{\partial A} = 12$ nF/cm^2, two order of magnitudes lower). Hence, by applying $V_G = -2$ V with an IL gate we can achieve a $\sigma_{\square,IL} = 1 \times 10^{13}$ holes per cm^2. By injecting such high charge densities, people have been able to achieve insulator-to-metal transitions[18,19] and even insulator-to-superconductor[20,21] transitions for the first time. IL gated organic polymer FETs have successfully been fabricated and showed an effective high hole doping density with

$|V_G| < 5$ V.[22–25] However, it was shown that one limitation of polymer semiconductors gated with ILs is that the FETs showed extreme hysteretic behavior (figure: 1.7(a)) due to the electrochemical mixing above certain V_Gs as schematically shown in figure 1.7(b).[26–28] In order to overcome this problem in organic polymer FETs we turn to single crystal organic FETs.
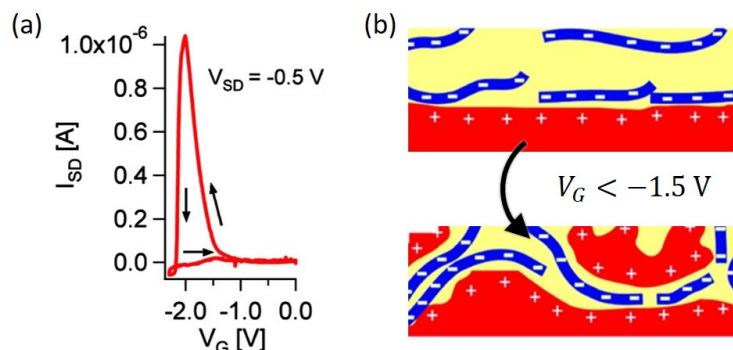
Figure 1.7: (a) The tranfer curve from a IL gated p3HT FET showing a hysteresis, the forward sweep in the V_G results in a sudden spike in current in the channel, attributed to the electrochemical mixing. (b) A illustration of the electrochemical mixing. Figures reprinted with permission from reference 26. Copyright 2010 American Chemical Society.

1.3 Monolayer MoS$_2$ - A 2D Semiconductor

1.3.1 Introduction to the Monolayer Semiconductor MoS$_2$

With the discovery of graphene in the 2000s, two-dimensional (2D) electronic materials have gained popularity with material scientists. The first class of 2D semiconductors were the transition metal dichalcogenides (TMDCs), derived from a class of layered Van der Waals materials. The TMDCs slipperiness makes them ideal lubricants, most commonly MoS$_2$ is used for this. Due to its 2D nature, monolayer MoS$_2$ is effectively all an interface: a perfect model system for studying semiconductor interfaces. Applying the scotch tape mechanical exfoliation method developed for graphene, researchers were able to achieve few-layer and monolayer MoS$_2$ (as seen in figure 1.8(b)) since the Van der Waals forces weakly hold the

layers together. A monolayer of MoS_2 consists of three atomic layers, the bottom and top a hexagonal grid of sulfur atoms and the middle layer is an offset hexagonal grid of molybdenum atoms as seen in figure 1.8(a).
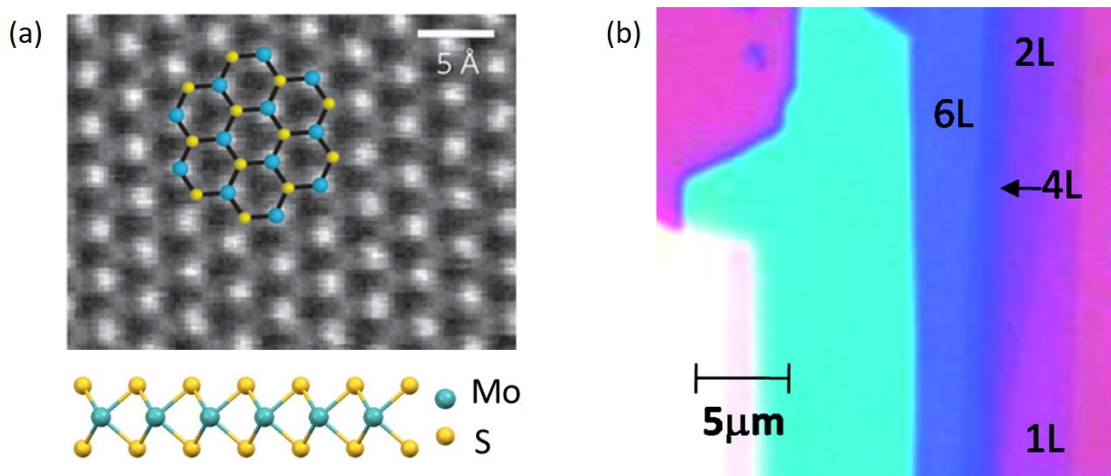
Figure 1.8: (a) A high-resolution ADF-STEM image of freely suspended monolayer MoS_2 on a TEM grid. The bright spots are molybdenum atoms; the grey spots are two stacked sulphur atoms. The lattice is composed of hexagonal rings alternating molybdenum and sulphur sites. A side illustration of the MoS_2 structure are overlaid at the bottom. Figure adapted by permission from Macmillan Publishers Ltd: Nature Materials, reference 29, copyright 2013. (b) An optical reflectance image of exfoliated MoS_2 on SiO_2 showing monolayer and few layer structure. Figures adapted with permission from reference 30. Copyright 2010 American Chemical Society.

1.3.2 Monolayer MoS_2 Electronic Band Structure

The seminal work of Mak *et al.* showed that by exfoliating MoS_2 to a monolayer the material went from a indirect to a direct semiconductor.[31] This is attributed to the fact that the valence band minimum at the Γ-point forms from the overlap of intralayer chalcogenide p_z orbitals (and Mo d orbitals), hence, in the absence of other layers to couple with the Γ-point possesses an energy below the K-point. The K-point electronic valence band energy relies on the interlayer coupling of the Mo d orbitals and is unaffected by the reducing MoS_2 to monolayer.[30] Figure 1.9(a) shows a density functional theory (DFT) with generalized gradient approximation (GGA) calculation of how the band structure of MoS_2 changes when moving from bulk to monolayer, resulting in the lowering of the Γ-point

energy. Experimentally this is observed by the sudden extreme photoluminescence (PL) enhancement when moving from a bilayer to monolayer MoS_2 as seen in figure 1.9(b).
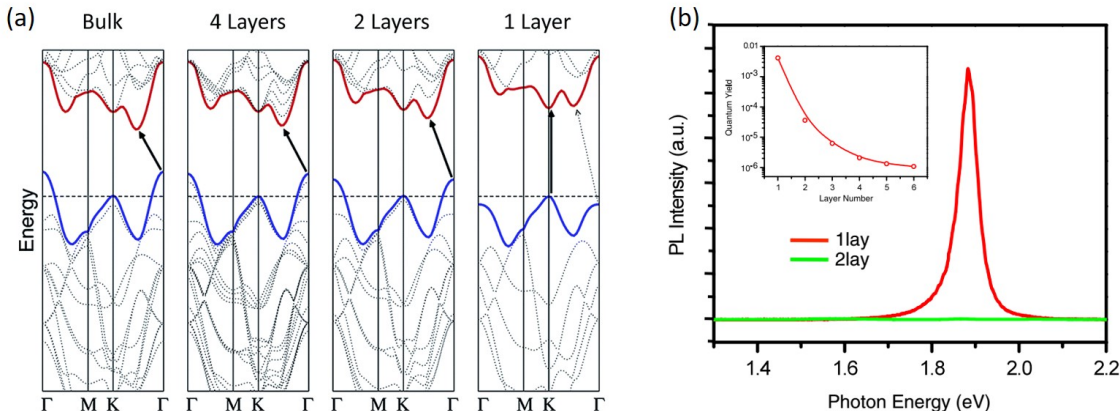
Figure 1.9: (a) Calculated band structures of bulk MoS_2, four layer MoS_2, bilayer MoS_2, and monolayer MoS_2. The solid arrows indicate the lowest energy transitions. Bulk MoS_2 is characterized by an indirect bandgap. With transitioning to monolayer thickness, the indirect bandgap becomes larger, while the direct remains unchanged becoming the lowest energy gap. An optical reflectance image of exfoliated MoS_2 on SiO_2 showing monolayer and few layer structure. Figures adapted with permission from reference 30. Copyright 2010 American Chemical Society. (b) Photoluminescence spectra of bilayer (green) and monolayer (red) MoS_2. The emergence of the bright peak at ~ 1.89 eV suggest the transition to a direct bandgap semiconductor at monolayer. The inset shows the PL quantum yield as function of layer thickness: showing many orders of magnitude increase as result of decreasing the number of layers of MoS_2. Reprinted figure (b) with permission from 31: Kin Fai Mak, Changgu Lee, James Hone, Jie Shan, and Tony F. Heinz, Phys. Rev. Lett., 105, 136805, 2010. Copyright 2010 by the American Physical Society.

1.3.3 Monolayer MoS_2: High Excitonic Binding Energy and Large Rashba Split

High Excitonic Binding Energy

Another unique electronic effect as a result of MoS_2 being reduced to a monolayer is the large excitonic binding energy observed.[32] Figure 1.10(a) shows the ionization potential of the excitonic state significantly lower than the conduction band (CB) minimum. Typically in inorganic materials the dielectric screening of the excitonic potential (which can by approximated as a hydrogenic species in the material with a dielectric constant of ε) is very large. This results in a very small binding energy (a few meV, much lower than room

temperature thermal energy). However, due to the majority of the excitonic field lines in a monolayer MoS_2 existing outside the material, the dielectric screening is dominated by the substrate and capping material - with free standing MoS_2 this is simply the permittivity of free space, ε_0 as illustrated in figure 1.10(b).
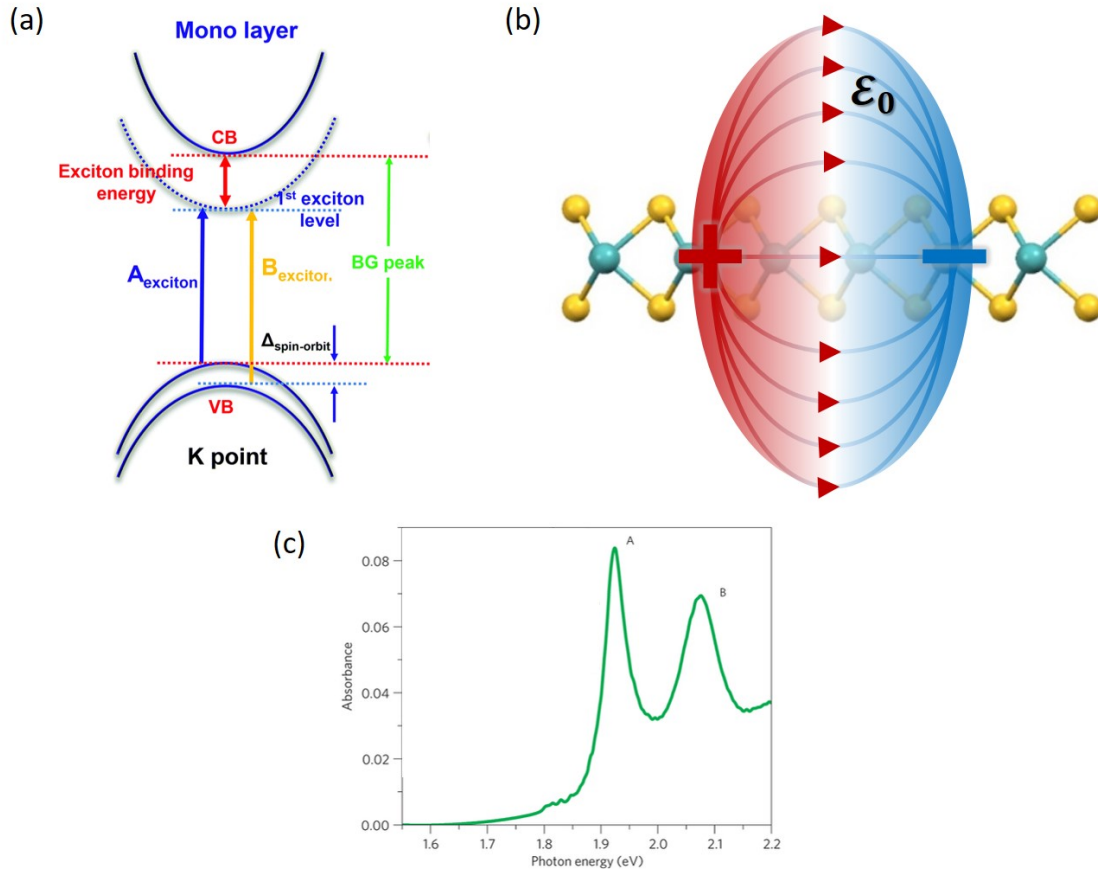
Figure 1.10: (a) The ionization potentials of the electronic states within monolayer MoS_2 and the corresponding optical transitions. The dotted line below the conduction band (CB) is the excitonic state with lower energy due to the excitonic binding energy. The two valence bands exist as a result of a Rashba split due to spin orbit coupling. Figure reprinted from reference 33 under the Creative Commons Attribution 3.0 Unported License. (b) An illustration of an exciton in MoS_2 showing the field lines which mostly exist outside the monolayer in a dielectric ε_0. (c) An absorption spectrum of monolayer MoS_2 showing the two exciton transitions (A and B) corresponding to the different Rashba bands. Reprinted by permission from Macmillan Publishers Ltd: Nature Materials, reference 34, copyright 2013.

Large Rashba Split

Figure 1.10(a) also illustrates the lower energy valence band (VB) having two subbands resulting from a Rasbha split in the MoS_2 band structure from the spin-orbit coupling

15

to the electronic states and the absence of inversion symmetry in the monolayer.[35] This is experimentally observed by the presence of a higher energy peak (typically referred to as the B-exciton in the literature and seen in figure 1.10(a)) in the PL spectra and absorption (shown in figure 1.10(c)) and the circularly polarized light selection rules.[34] This has generated interest in a new paradigm of (opto-)electronic devices based on spin, called spintronics or valleytronics.[35]
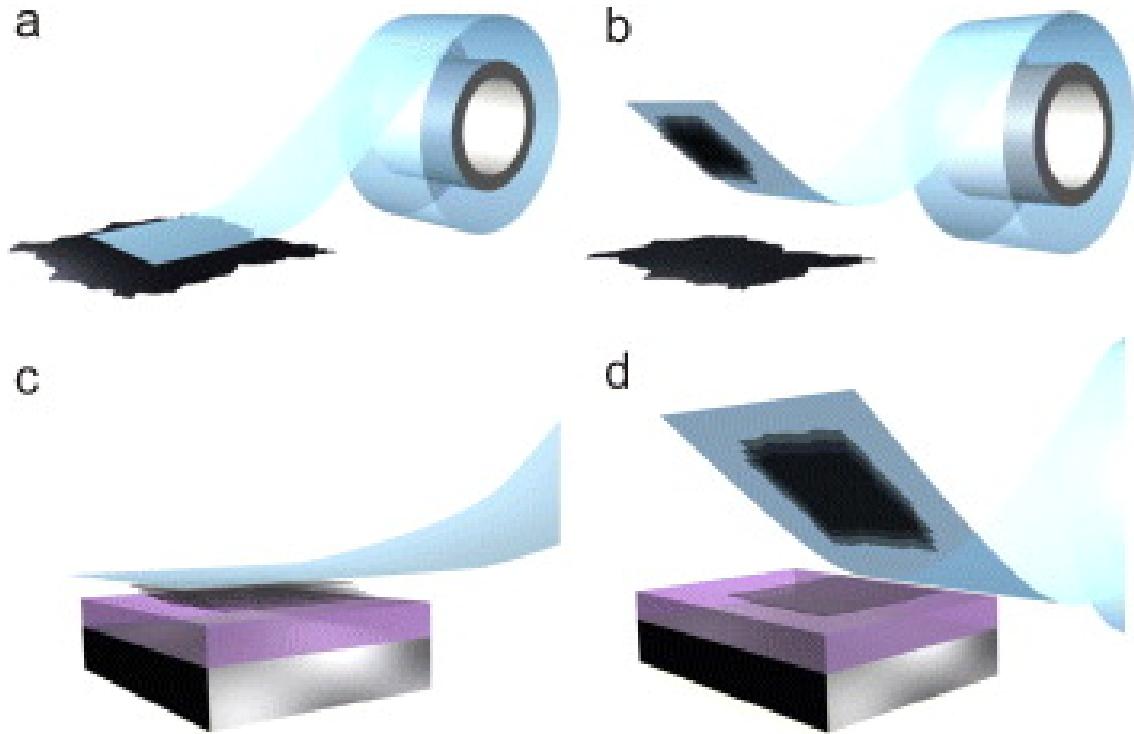
Figure 1.11: The procedure of mechanically exfoliating a material using scotch tape: (a) & (b) Scotch tape is used to pick up a few layers of the layered material then (c) the scotch tape with the layer material is pressed against a new substrate and (d) a monolayer from that material is left behind. Figure reprinted from reference 36, ©of The Royal Swedish Academy of Sciences. Reproduced by permission of IOP Publishing. All rights reserved.

1.3.4   Production of Monolayer Semiconductor MoS$_2$

While achieving 2D electronic materials has been of interest to scientists for a long time, fabricating large enough crystals to investigate has been a large barrier to the pursuit of such studies. The work of Novoselov and Gaim on mechanically exfoliated graphene

monolayers opened the door to research on large (i.e. > 1 μm^2) single crystals of 2D materials.[37] However, a practical limitation to exfoliation is the limited yield of 2D samples and still prohibitively small sizes for commercial application. To overcome this, chemical vapor deposition (CVD) has been developed in order to produce wafer scale amounts of monolayer MoS$_2$ making the prospect of 2D devices much more commercially viable.[29]

Mechanical Exfoliation

The typical scotch-tape mechanical exfoliation process is illustrated above in figure 1.11. Bulk MoS$_2$ is stuck on a piece of scotch tape which is then repeatedly folded and unfolded resulting thin flakes on the tape's adhesive surface. Then the tape is pressed onto cleaned Si:SiO$_2$ substrates. After mild rubbing, the tape is peeled from the substrate, yielding some monolayer MoS$_2$ flakes. The size of single layers ranged from 1 to 10 μms.[31] An example of exfoliated MoS$_2$ is shown in 1.8(b).

Chemical Vapor Deposition
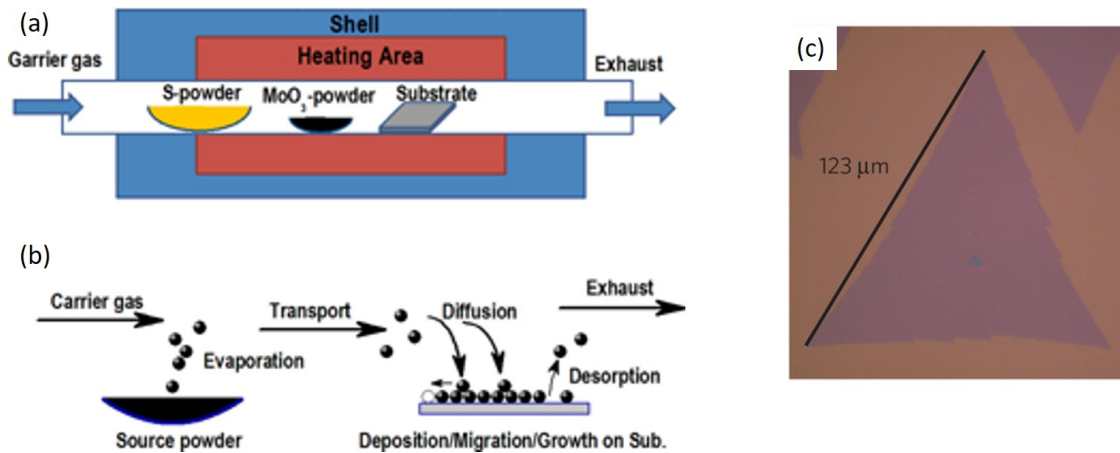
Figure 1.12: (a) An illustration showing one method of CVD growth of MoS$_2$ in which a furnace with a carrier gas takes the S and Mo and deposits them on the substrate in a cooler area to form the monolayer MoS$_2$. (b) A schematic of the hypothesized mechanism of the CVD method in (a). Figures (a) and (b) reprinted from 38, with the permission of John Wiley and Sons Publishing. (c) An optical microscope image of a CVD grown MoS$_2$ monolayer. Figure reprinted by permission from Macmillan Publishers Ltd: Nature Materials, reference 29, copyright 2013.

CVD growth of monolayer MoS_2 has been developed for growing both wafer sized polycrystalline films and large monolayer single crystal triangular flakes.[29] An illustration of the setup is shown in figure 1.12(a). Figure 1.12(b) shows the proposed mechanism of the CVD process.[38] Cleaned Si:SiO₂ substrates were placed at the center of a furnace beside a MoO_3-covered silicon substrate. ~ 1 g of sublimated sulfur was placed at the opening of the furnace where the sulfur reached an approximate maximum temperature of 600°C. The center of the furnace was heated to 550°C over a period of 30 min (20°C/min) with a nitrogen flow rate of 200 sccm. The furnace was then heated to 850°C at a slower pace of $\sim$ 5°C /min. After sitting at this temperature for 10-15 minutes, the furnace was allowed to cool naturally back to room temperature yielding the monolayer MoS_2 triangular flakes as seen in figure 1.12(c).
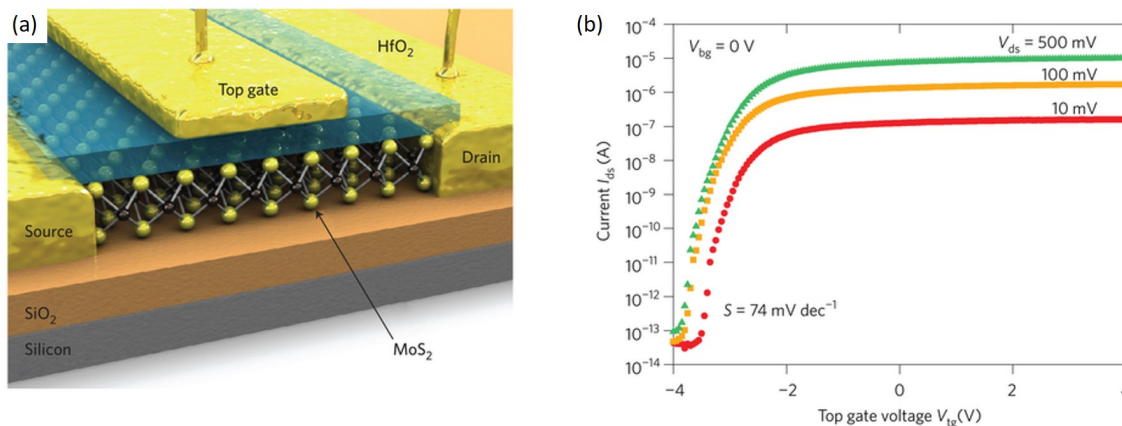
Figure 1.13: (a) An illustration of an HfO_2 top gated MoS_2 FET. (b) shows the corresponding FET transfer curves at room temperature in the saturation regime. Figures reprinted by permission from Macmillan Publishers Ltd: Nature Nanotechnology, reference 39, copyright 2011.

1.3.5 Monolayer Semiconductor MoS_2 FETs

Monolayer MoS_2 has shown promising uses in the fields of (opto-)electronics,[40–42] photonics,[43] spintronics,[35] sensors,[44,45] catalysis[46,47] and energy storage.[48] FETs are of particular interest as they show the charging and transport properties of MoS_2. Figure 1.13(a) shows a schematic of HfO_2 gated monlayer MoS_2 FET and (b) shows the corresponding transport

properties.[39] The mobility does show the bandlike behavior ($\frac{\partial \mu}{\partial T} < 0$) as expected; however the mobility is typically only hundreds of $cm^2V^{-1}s^{-1}$ at room temperature. This is far lower than the predicted mobility of thousands of $cm^2V^{-1}s^{-1}$. It is thought that the mobility is limited by the contact resistance made to the MoS_2 channel as well as the extensive number of defects found in the material (to be discussed in a later chapter). Mitigating defects and improving the mobility of 2D TMDCs is one of the biggest challenges that needs to be addressed in the fabrication of 2D semiconductor devices.
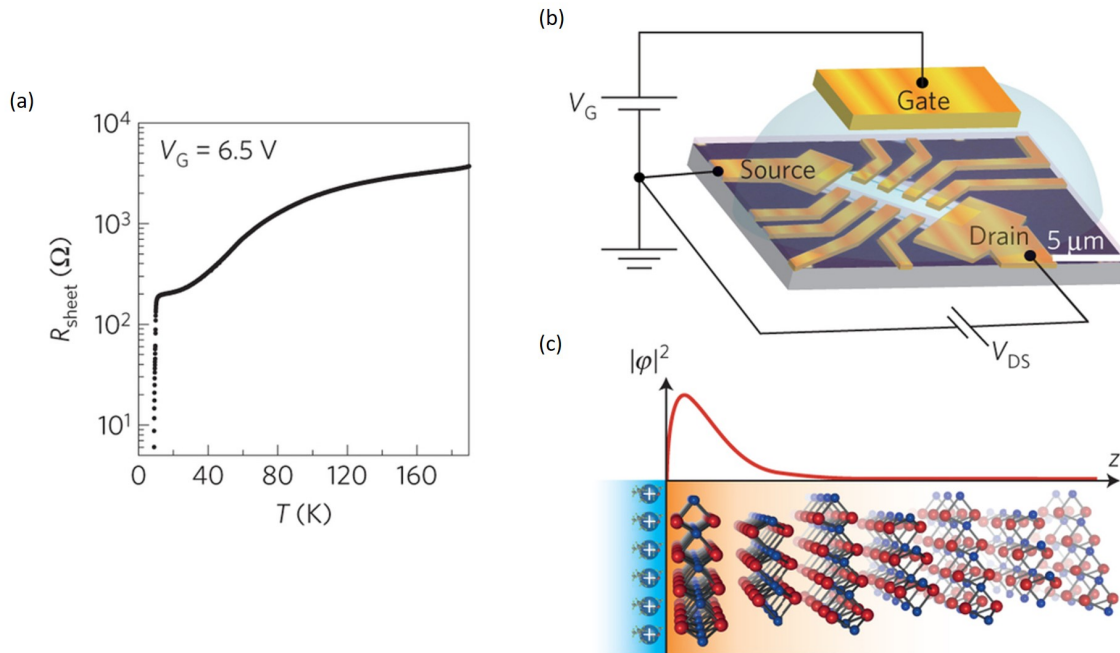
Figure 1.14: (a) Plot of an IL gated few layer MoS_2 FET sheet resistance as a function of temperature showing a transition to superconductivity at around $T = 10$ K. (b) Illustration of the IL top gated MoS_2 FET used to achieve superconductivity seen in (a). (c) Schematic of the electric double layer at the IL/MoS_2 interface and the corresponding electric potential within the MoS_2 resulting in a high enough charge density to achieve superconductivity. Figures reprinted by permission from Macmillan Publishers Ltd: Nature Physics, reference 49, copyright 2015.

IL Gated Superconducting MoS_2

As with rubrene, IL was used as a gating dielectric in order to achieve high charge densities within MoS_2. Recent work by several research groups has shown that using an IL gate (the FET is schematically shown in 1.14(b)) superconductivity can be achieved in

monolayer MoS_2 as displayed in the plot in figure 1.14(a).[49–51] This is due to the electric double layer formed at IL/MoS_2 interface as illustrated in figure 1.14(c).

The ability for IL to form an electric double layer at the MoS_2 surface lends itself to the hypothesis that it may be able to passivate existing charges at the surface - mitigating their trapping effects. An idea shown to work in rubrene by Lee *et al.* using a dipolar liquid.[52]

Chapter 2

Negative Transconductance in Ionic Liquid Gated Rubrene Field Effect Transistors

As mentioned previously single crystal rubrene shows relatively high mobilites (> 10 cm^2 V^{-1} s^{-1})and bandlike transport. To overcome the high applied voltages needed in an organic FET, using an IL dielectric with rubrene is an appropriate strategy. Furthermore, being a well ordered single crystalline semiconductor, electrochemical mixing with the IL is less favorable. However, when implementing the IL gated rubrene FET unconventional behavior is observed:
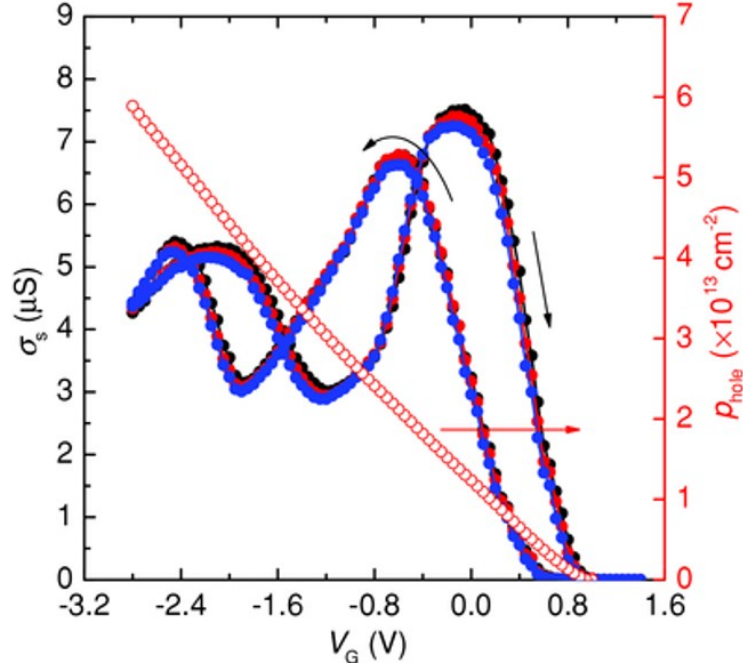
Figure 2.1: The left axis corresponds to the sheet conductance, σ_S, as a function of gate voltage, V_G, over three consecutive sweeps for a rubrene IL gated at $T = 225$ K. Both forward and reverse sweeps are shown. The right axis and red open circles shows the hole density, p, as a function of V_G. Figure reprinted from 53, with the permission of John Wiley and Sons Publishing.

2.1 Negative Transconductance: Decreasing Mobility With Increasing Charge Density

Figure 2.1 clearly shows the unusual behavior of the IL gated rubrene FET: the conducitivity, σ_s in figure 2.1(a) drops when a more negative gate voltage is applied below $V_G = -0.1$ V, so even though this results in an increasing hole density at the IL/rubrene interface. This suggests that *as the density of holes increases the charges move more slowly.* Of course this is extremely unfavorable for the commercial viability of the IL gated rubrene FET. In order to mitigate such FET behavior it is necessary to understand why this happens.

The hypothesis made by Xia *et al.* and then by Xie *et al.* was that beyond some threshold charge density, the holes start to become localized in rubrene leading to two types of conductive channels, one fast bandlike channel and another slow, thermally-activated

hopping channel.[17,53,54] As the hole density increases the holes localize and the hopping channel becomes more dominant resulting in a decreasing conductance. The second peak in the mobility was attributed to an optimal hole density which favors site-to-site hopping. High densities result in too few sites for the holes to hop to since so many are filled at high densities which then results in a drop in the conductance again (i.e. this is a basic two dimensional percolation model). They showed that qualitatively this model showed a similar behavior as was observed in the IL gated rubrene FETs. However, they were unable to confirm this hypothesis using electrical transport methods - direct evidence for the nature of the carriers was still missing and is required to test the model. IR spectroscopy is able to access directly the nature of the charge carriers in the rubrene at the IL interface.

2.2   Ionic Liquid Gated Rubrene Devices

2.2.1   PDMS Stamps IL Rubrene FETs

Fabricating IL gated single crystal rubrene FETs is similar to the method used for air gated FETs, except the air gap is filled with an IL dielectric. A master pattern is made on a substrate using photolithography and wet polydimethylsiloxane (PDMS) is poured onto the patterned substrate and allowed to dry. The dry PDMS is then removed possessing raised pads of height, d, corresponding to the distance from the gate electrode and the semiconductor. The pads are separated by a distance, L, corresponding to the FET channel length. Then, 2 nm of Ti (or Cr, as a sticking layer) followed by up to 15 nm of Au are deposited on the PDMS to serve as Ohmic contacts to the semiconductor. The rubrene single crystal is then laminated on the top of the two raised pads completing the air gap FET as shown in figure 1.5 (a). Finally, a drop of IL is placed in the gap between the raised pads next to the rubrene crystal and the IL is drawn under the crystal by capillary action completing the IL gated rubrene FET. A top down image of the device is shown in figure

2.2(a) and (b) shows a cross-sectional schematic of the IL gated rubrene FET.[17]
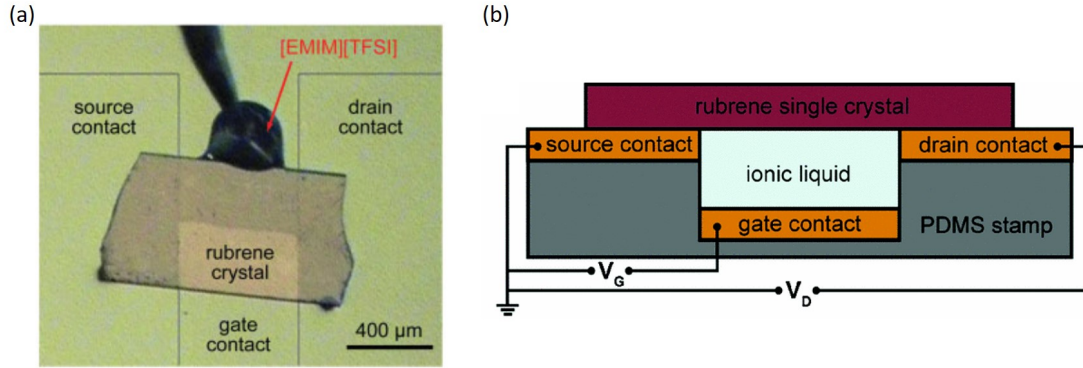
Figure 2.2: (a) An optical microscope image of a PDMS stamp IL gated rubrene FET from reference 55. Figure (a) reprinted from 55, with the permission of John Wiley and Sons Publishing. (b) A schematic showing the cross-section of the PDMS stamp IL gated rubrene FET. Reprinted figure (b) with permission from 17: Yu Xia, Wei Xie, P. Paul Ruden, and C. Daniel Frisbie, Phys. Rev. Lett., 105, 036802, 2010. Copyright 2010 by the American Physical Society.

2.2.2   Ion Gel Gated Rubrene MIS Capacitors

While an FET can be used to study the charging of the IL/rubrene interface, a MIS capacitor geometry is also sufficient. Employing a side-gated geometry with a ion gel (IG) instead of an IL allows for the elimination of the Fabry-Pérot interference in the gap which the IL exists.

Ion Gel

An IG typically is fabricated as a polymer electrolyte film, with charged side-chains on a polymer mixed with mobile counter-ions (shown in figure 2.3(a)).[56] Hence, due to the mobile ions the IG has a similar high dielectric constant as an IL, with the added benefit of having control over the shape of the dielectric (i.e. removing the disadvantages of having a liquid). However, some IG developed are simply IL intercalated in a polymer matrix (shown in figure 2.3(b)). This is analogous to a sponge which can hold the IL but inhibit its liquid-like behavior by constraining it to its solid polymer shape. These IGs can be "cut-and-stuck"

24

onto any location.[57]
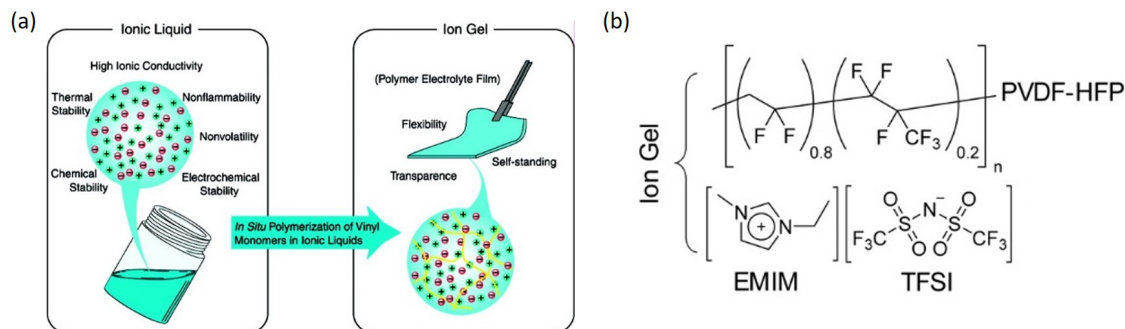
Figure 2.3: (a) A comparison of ionic liquids and ion gels showing how the strengths of ILs are possessed by IGs. Figure adapted with permission from reference 56. Copyright 2005 American Chemical Society. (b) an example of a ion gel which is a mixture of a fluoropolymer and an IL.[57]

Ion Gel Preparation:[57] Poly(vinylidene fluoride-co-hexafluoropropylene) (PVDF-HFP) (M_n = 130000 g·mol^{-1} and M_w = 400000 g·mol^{-1}) and 1-ethyl-3-methylimidazolium bis (trifluoromethylsulfonyl)amide were codissolved in acetone at 60 °C in a 1:4:6 mass ratio of the respective components. The warm solution was spun at 1200 rpm for 1 min onto a 2 cm × 2 cm glass slide made rough by sanding. The composition of the resultant film is likely different from the original solution. The coated slide was then baked in a vacuum overnight at ∼ 70 °C and stored in a glovebox before being used in the device fabrication. The resulting ion-gel was smooth on one side (for contacting rubrene) and rough on the other side (to avoid interference artifacts in optical spectroscopy).

IG Side Gated Rubrene MIS Capacitors

Capacitor Fabrication: (Illustrated below in figure 2.4.) Previously selected rubrene crystals grown by physical vapor transport were masked and partially metalized with 40 nm of Au (Base pressure ≤ 5×10^6 Torr and deposition rate ∼ 1 Å · s^{-1}), leaving part of the rubrene (001) crystal surface exposed. The rubrene crystal was then glued or taped on a glass or silicon substrate covered with 100 nm of Au (with a 3 nm adhesion layer of Cr) as the other electrode for the capacitor and a back mirror for IR spectroscopy. A 1 mil Au wire
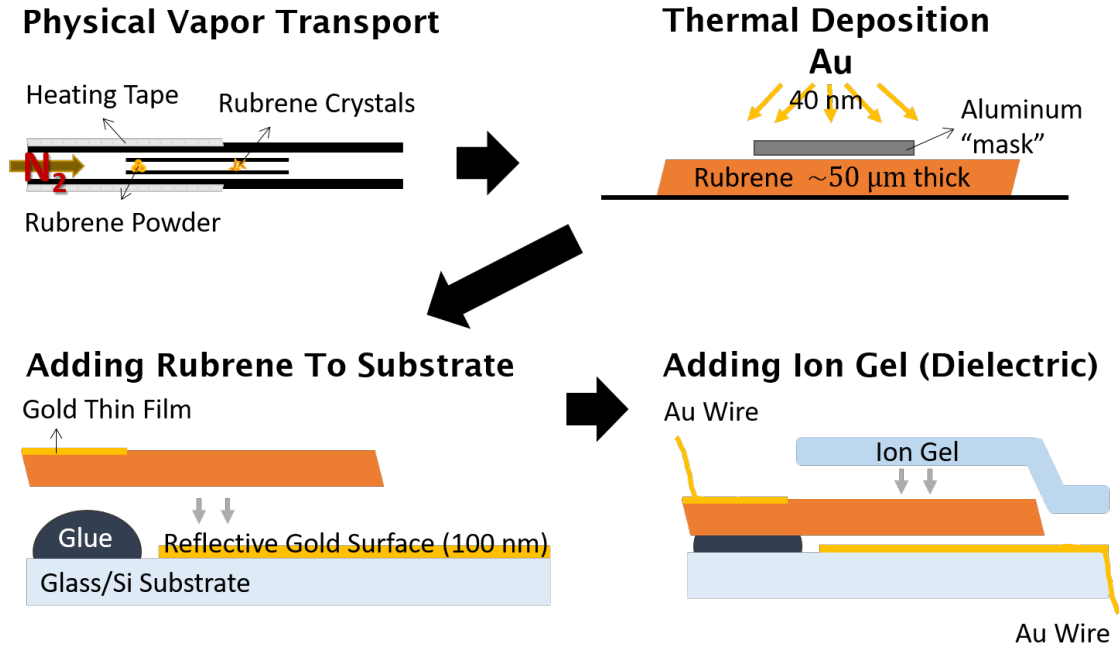
Figure 2.4: The fabrication scheme used to make IG gated rubrene MIS capacitors for IR spectroscopy measurement. First the rubrene single crystals are grown using a physical vapor transport method. Then gold electrodes are deposited onto part of the crystal, leaving the other part blank as a channel. The rubrene with the gold electrodes is glued to a substrate with a gold film on as a gate electrode and mirror for IR reflectance measurements. Finally, the electrodes are contacted with gold wire and an ion gel is laminated on top.[58]

was then adhered to the Au on the rubrene crystal via graphite or silver conductive paste (Ted Pella) and another wire was adhered to the gold-covered substrate by conductive paste. A piece of the rough ion gel was cut from the roughened slide using a scalpel and laminated on both the gold substrate and bare rubrene crystalline surface using tweezers. The gold was covered with graphite conductive paste for the graphite capacitor electrode. A microscope image of a completed MIS device is illustrated below in figure 2.5(a).

MIS Capacitor Effective Circuit: During the measurement the fabricated IG gated rubrene MIS capacitor was put in series with a known high resistance, R, and the electrical measurements were made with a Keithley 6517A Electrometer. Using the current flowing through the circuit as function of time, $I_G(t)$, (shown in figure 2.5(c)) the contact resistance, R_C and the leakage resistance, R_L were extracted given the following equations derived from
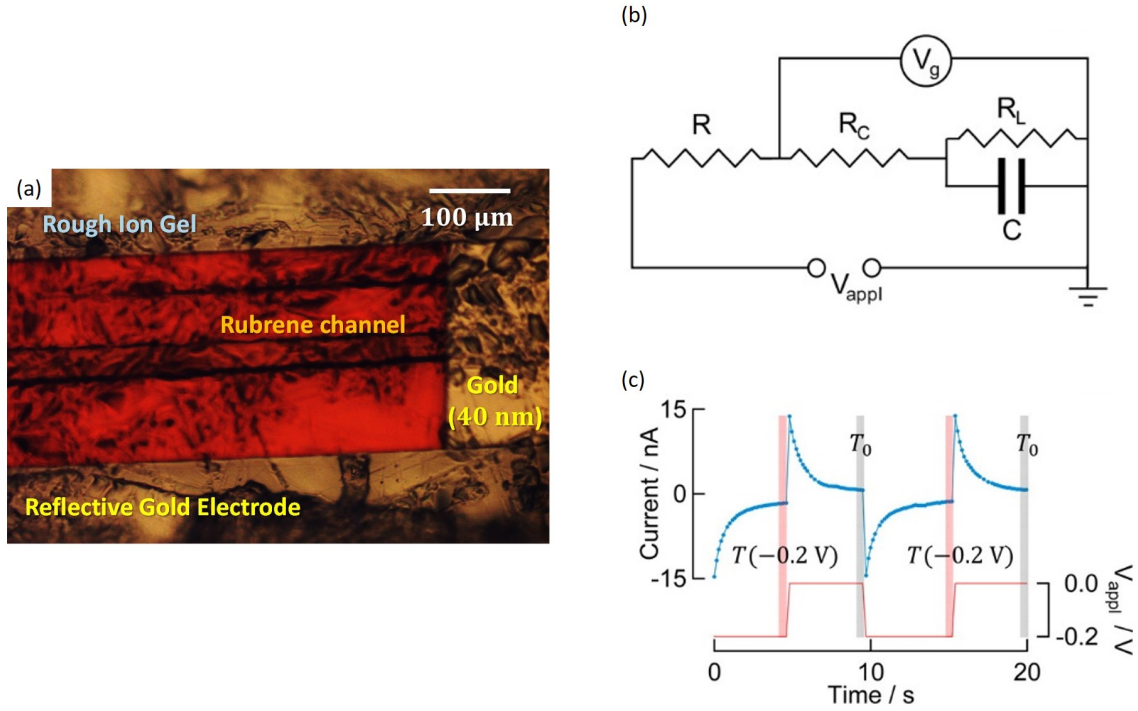
Figure 2.5: (a) An optical microscope image of a IG gated rubrene MIS capacitor, IG is roughened to minimize any Fabry-Pérot interference in the IR spectrum. (b) The equivalent circuit of the electrical connections made to the IG gated rubrene MIS capacitor, with a known resistor, R, in series and accounting for contact resistance, R_C, and leakage current in R_L as well as the capacitance, C. (c) The capacitor charging current as function time (on the left axis) and the corresponding applied voltage, $V_{applied}$ as function time. Figure (b) and (c) reprinted with permission from reference 58. Copyright 2015 American Chemical Society.

basic electrical circuit theory:[12]

$$R_C = \left(\frac{V_g - V_R\,(t = 0\text{ s})}{V_R\,(t = 0\text{ s})}\right) R \tag{2.1}$$

$$R_L = \left(\frac{V_g - V_R\,(t \to \infty)}{V_R\,(t \to \infty)}\right) R - R_C \tag{2.2}$$

Hence, the $R_C \sim 2\ M\Omega$, effectively negligible compared to $R_L > 0.2\ G\Omega$. We can also extract the capacitance C from the figure 2.5(c) which shows a $I_G\,(t)$ over several cycles of charging and discharging the capacitor with sharp steps in the gate voltage. We obtain the total injected charge density, $\Delta\sigma_E$, from the charging and discharging parts of the I/V curve as $\Delta\sigma_E = (1/A) \int I\,(t)\,\mathrm{d}t$, where A is the interface area between rubrene and ion-gel

27
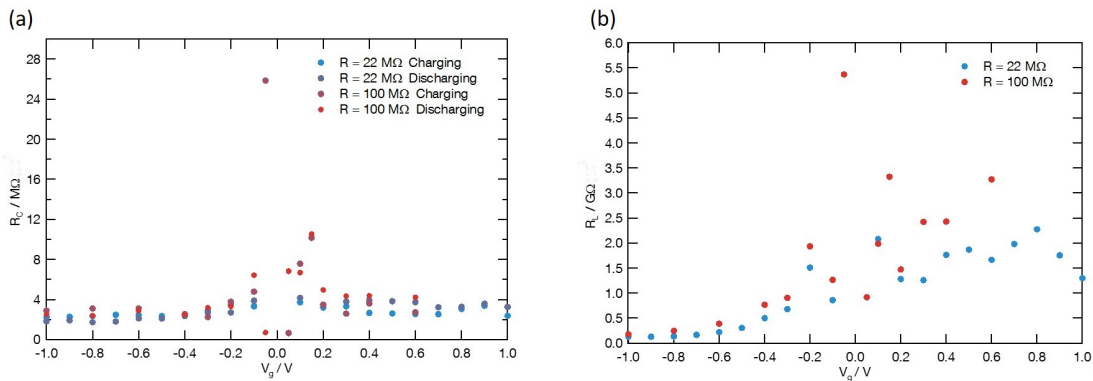
Figure 2.6: (a) Plot of contact resistance, R_C, as function of applied voltage, V_g, obtained from initial charging and discharging potential drops, $V_R\,(t = 0\,\mathrm{s})$, across a known resistor, R, and calculated using equation 2.1. (b) Plot of contact resistance, R_L, as function of applied voltage, V_g, obtained from final charging and discharging potential drops, $V_R\,(t \to \infty)$, across a known resistor, R and calculated using equation 2.2. Figures reprinted with permission from the supplementary material of reference 58. Copyright 2015 American Chemical Society.

and $I\,(t)$ is the current. As we show below in Figure 3.5, a plot of $\Delta\sigma_E$ versus V_g shows a linear relationship, which gives a specific capacitance of $C = 8 \pm 3\ \mu\mathrm{F} \cdot \mathrm{cm}^{-2}$, in agreement with reported values.[57]

Chapter 3

Charge Saturation and Intrinsic Doping in Electrolyte-Gated Organic Semiconductors

[58] As mentioned previously Frisbie and co-workers demonstrated negative transconductance in IL gated rubrene at a doping level of 10^{13} holes per cm^2.[17,53,54] These authors attributed the anomalous transport behavior to carrier localization at high doping densities, but the physical nature of the interface remains unclear. Hence, we turn to IR spectroscopy to uncover details at the IL/rubrene interface.

Specifically charge-modulated Fourier transform infrared (CM-FTIR) spectroscopy[59–61] is ideal to uncover the nature of electrolyte-gated doping of organic semiconductors at the model interface between single-crystal rubrene and ion gel (IG). FTIR spectroscopy has been used before to great success in unveiling the band-like transport and low effective mass of holes injected into single crystal rubrene at lower charge densities ($\sim 10^{12}$ holes per cm^2) with SiO_2, parylene, or poly(para-xylylene) as dielectrics.[59–61] IR spectroscopy is sensitive to the unique signatures for bandlike transport (the Drude peak)[59] or thermally activated

transport for localized polaronic species in the semiconductor[15] as well as sensitivity to vibronic coupling to the charged species.[28]

It is natural to apply CM-FTIR to study rubrene at a higher doping density enabled by electrolyte gating. The ability to optically monitor charge (hole) density in the organic semiconductor, in conjunction with electrical measurements, allows us to make two discoveries. First, we show that a high surface hole density ($\sim 2 \times 10^{13}$ cm^{-2}), as measured from the free-carrier like hole absorbance in CM-FTIR spectroscopy, is formed in the organic semiconductor upon formation of the ion-gel/rubrene interface, in the absence of gate bias. Applying a positive gate voltage, $V_{appl} > 0$ V, we extract the free-carrier like holes introduced by this intrinsic doping. Second, we find that with an increasingly negative applied voltage, the change in surface free-carrier like hole density measured by optical absorption, $\Delta\sigma_{IR}$, reaches a plateau at $\sim 3 \times 10^{13}$ holes cm^2, while the injected total charge density determined electrically, $\Delta\sigma_E$, continues to rise linearly. This saturation in the free-hole density on the rubrene crystal correlates well with the drop in conductance observed in transport measurements.[17,53]

3.1 Charge-Modulated Fourier-Transform Infra-Red Microspectroscopy

The devices were fabricated from single crystals of rubrene as described in the previous chapter. In the CM-FTIR spectroscopic experiments, we apply a voltage between the two metallic contacts and measure the charging and discharging characteristics of the capacitor by electrical methods, while simultaneously measuring the IR absorbance spectra of the ion-gel/rubrene structure. Figure 3.1(a) shows the sample design and the experimental setup, and Figure 3.1(b) shows the equivalent electrical circuit. Because the leakage resistance (R_L) through the device is $1 - 2$ orders of magnitude higher than other resistances in the circuit,
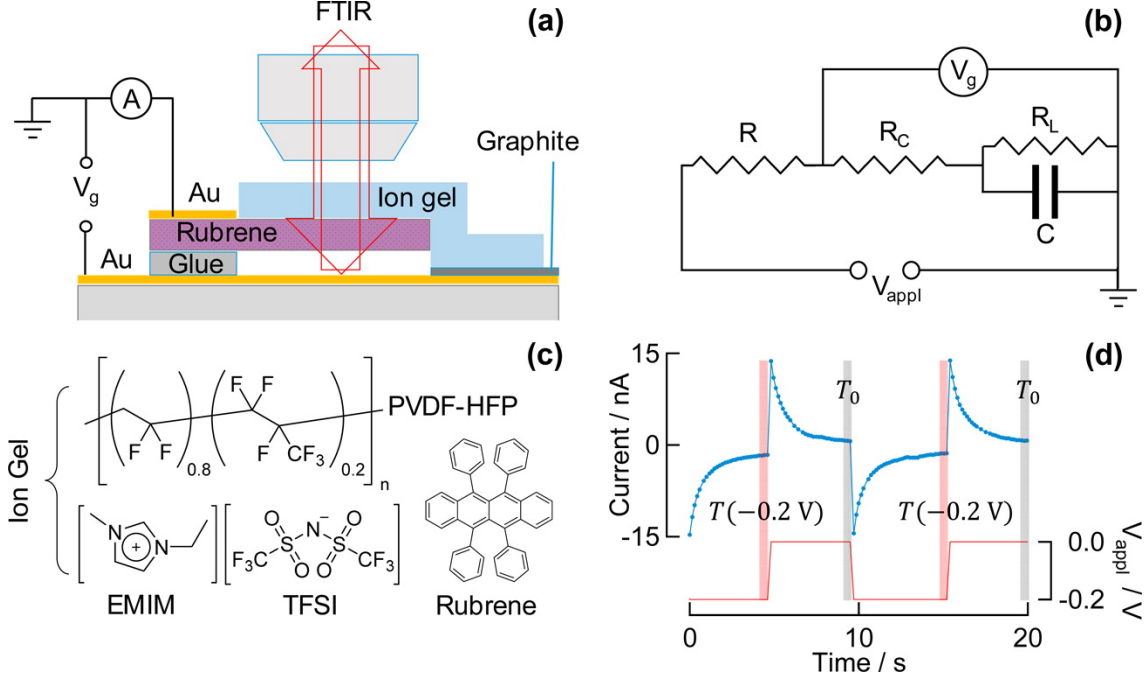
Figure 3.1: (a) Sample setup for the CM-FTIR experiment: A 40 nm Au thin film is deposited onto part of a rubrene crystal via a shadow-mask. The sample is glued and spaced from a gold electrode/mirror substrate (100 nm Au on glass). A piece of ion-gel is placed on top of the exposed rubrene [001] surface, and part of the ion-gel is electrically contacted to the Au mirror with or without graphite paste. The device is connected with gold wires to a Keithley 6517a voltage source and electrometer. IR light is focused onto the device and, after reflection from the Au mirror, repasses through the device and directed to the detector. (b) The equivalent circuit of the device. The applied gate voltage, V_{appl}, is from the Keithley 6517a, which also gives total current. A known resistor, $R = 11$ MΩ, is used in series with the ion-gel/rubrene capacitor. Quantitative modeling of the device gives a leakage resistance through the capacitor of $R_L = 1.0-0.2$ GΩ (for $V_{appl} = -0.1$ to -0.8 V) and a negligible contact resistance of $R_C \sim 2$ MΩ (SM1). (c) Molecular structures of the ion gel and of rubrene. The ionic liquid consists of 1-ethyl-3-methylimidazolium (EMIM) cations and bis(trifluoromethylsulfonyl)amide (TFSI) anions. The polymer matrix is poly(vinylidene fluoride-co-hexafluoropropylene) (PVDF-HFP). (d) The upper, blue graph shows the current, $((V_{appl} - V_g)/R)$, flowing through R for two charging ($V_{appl} = -0.2$ V) and discharging ($V_{appl} = 0$ V) cycles. The lower, red graph shows the applied voltage, V_{appl}, of the corresponding cycles. The light red shade corresponds to when an CM-FTIR spectrum, $T(-0.2$ V$)$, is acquired after charging, while the gray shade corresponds to when an CM-FTIR spectrum, T_0, is acquired after discharging. Figures reprinted with permission from reference 58. Copyright 2015 American Chemical Society.

we have $V_g \approx V_{appl}$ in the steady-state and there are negligible electrochemical effects, i.e., no charge transfer between the rubrene and IG. Figure 3.1(c) illustrates the molecular structure of the ion-gel and rubrene.

A Nicolet 6700 FTIR with a KBr beam splitter and Everglo IR light source coupled to a Continuum IR microscope in reflection mode with a MCT-A detector and a Reflectochromat 15× objective was used. Sample was kept in a home-built, actively nitrogen-purged cell

with a KBr window. The FTIR was controlled using OMNIC 9 software with an in-house written Omnic Macro to interface with the Keithley Labview executable to allow for charge modulation measurements.

In order to resolve the change in Mid-IR absorption induced by charging the rubrene a charge modulation technique was employed. All spectra obtained, $T_{V_g}(\omega)$, are an average of 4 spectra taken in under 1 s (within the limits of the instrument response time). FTIR spectra, $T_{0\,V}(\omega)$, were obtained after waiting 3 s with $V_g = 0$ V to make sure the device was completely discharged (shown in figure 3.1(d) by the grey bar), and then a known, fixed bias was applied, $V_{applied}$, for 3 s (shown in figure 3.1(d) by the red bar) to ensure the rubrene was completely charged before obtaining another spectrum, $T_{V_g}(\omega)$. This yields a total charging and discharging period, $T_{CMS} \sim 8$ s. A change in optical density ΔOD due to charging was obtained for this pair of spectra by:

$$\Delta\text{OD} = 1 - \frac{T(V_g)}{T_0} \tag{3.1}$$

Figure 3.2 illustrates the process. This process was then repeated 200 more times with frequency, $f_{CMS} = \frac{1}{T_{CMS}} \sim 0.1$ Hz and an averaged ΔOD is obtained:

$$\langle \Delta\text{OD}(\omega, V_g) \rangle = \frac{1}{200} \sum_{i=1}^{200} \left(1 - \frac{T_{V_g}(\omega)}{T_{0\text{V}}(\omega)} \right)_i \tag{3.2}$$

where i is the iteration number. Similarly a standard error of the mean was extracted:

$$SE_{\langle \Delta\text{OD}(\omega, V_g) \rangle} = \frac{1}{200} \sqrt{ \sum_{i=1}^{200} \left(\left(1 - \frac{T_{V_g}(\omega)}{T_{0\text{V}}(\omega)} \right)_i - \langle \Delta\text{OD}(\omega, V_g) \rangle \right)^2 } \tag{3.3}$$

To account for any drift in the baseline of the system response such that $\langle \Delta\text{OD}(\omega \to \infty, V_g) \rangle \neq 0$ (shown in figure 3.3), a constant, K, was subtracted from $\langle \Delta\text{OD}(\omega, V_g) \rangle$:
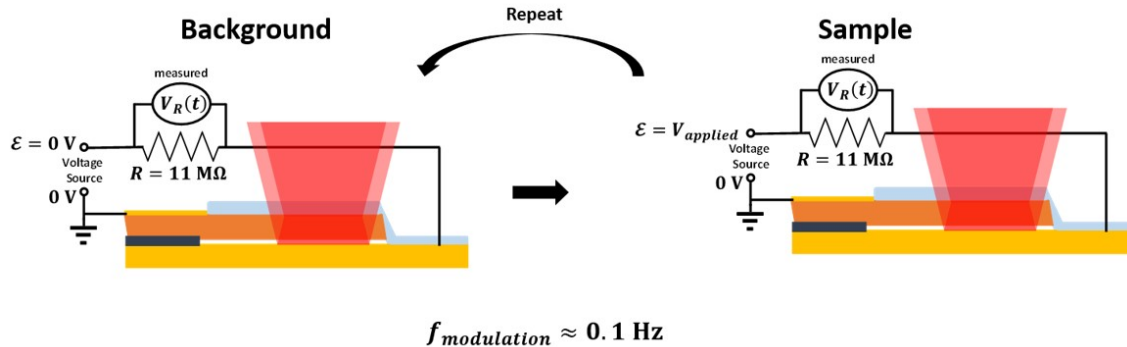
Figure 3.2: A schematic of the charge modulated Fourier transform IR spectroscopy on the IG gated rubrene capacitor, showing the acquisition of the IR spectrum when no gating bias is applied and then the acquisition after charge injection when a electromotive force, $\mathcal{E} = V_{applied}$ is applied. The repetition of the process at 0.1 Hz.[58]

$$\langle \Delta \text{OD} \left(\omega, V_g \right) \rangle_{corrected} = \langle \Delta \text{OD} \left(\omega, V_g \right) \rangle - K \tag{3.4}$$
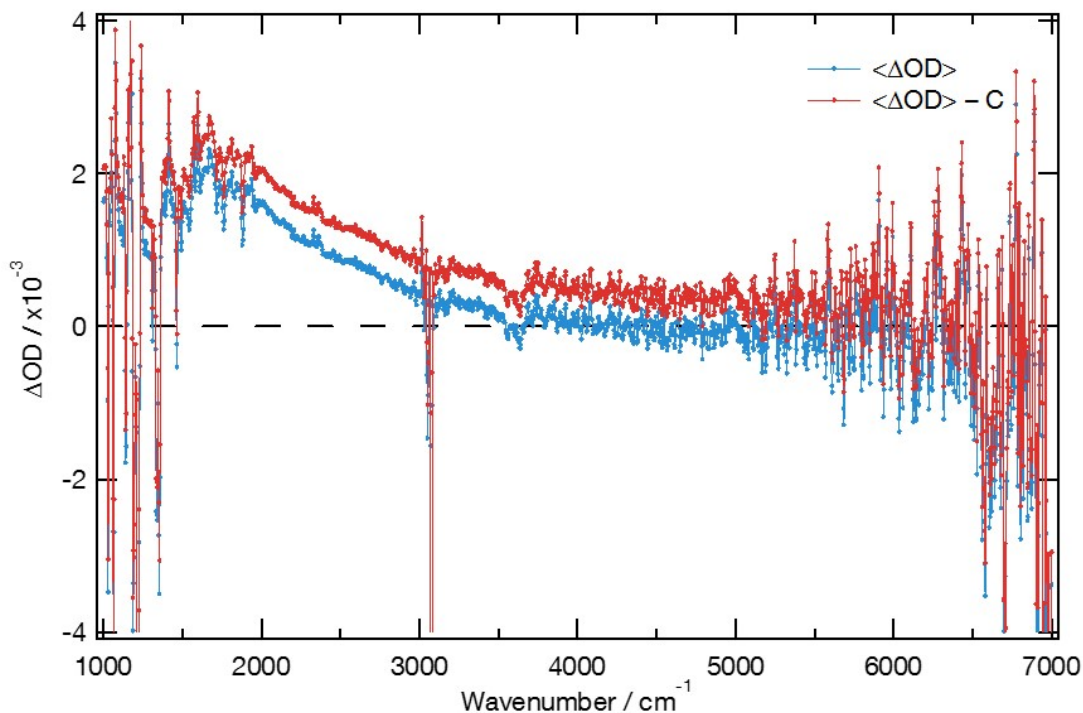
Figure 3.3: Plot of change in optical density, ΔOD, as a result of charging at $V_g = -0.5$ V function of wavenumber. The blue dots show the raw data and the red dots show the corrected data with $C = -4.3 \times 10^{-4}$. Figures reprinted with permission from the supplementary material of reference 58. Copyright 2015 American Chemical Society.

K was obtained by fitting the spectrum $\langle \Delta \text{OD} \left(\omega, V_g \right) \rangle$ (neglecting areas with vibrational

peaks) with the equation:

$$f(\omega) = \frac{A}{\omega^2} + K \qquad (3.5)$$

where A and K were allowed to vary as free parameters to the fit. K took values on the order $\leq |10^{-4}|$ and could be positive or negative and show no correlation with V_g. Henceforth, $\langle \Delta \mathrm{OD}(\omega, V_g) \rangle_{corrected}$ is represented by $\Delta \mathrm{OD}(\omega, V_g)$.

For negative applied bias ($V_g < 0$ V), we see an induced absorption ($\Delta \mathrm{OD} > 0$) over a wide spectral range, with a magnitude that increases with decreasing wavenumber. This is an optical signature qualitatively consistent with Drude absorption ($\propto 1/\omega^2$, where ω is the light frequency) of free carries, as observed and analyzed previously for free-carrier like holes in rubrene gated with other gate-dielectrics.[59–61] Due to the limited spectroscopic window here, we do not attempt to fit the broad spectral feature (rising $\Delta \mathrm{OD}$ with decreasing ω) to the Drude equation, but only to quantify the hole intensity from the absorbance. With increasingly negative bias, the IR absorption increases, in proportion to the amount of injected holes.[62]

For positive bias, we expect the rubrene to be depleted of holes and hence the IR spectrum to remain unchanged with respect to $V_g = 0$. On the contrary, we find that this bias regime exhibits bleaching, which precisely mirrors the induced-absorption features seen for $V_g < 0$ V. This bleaching shows that free-carrier like holes are already present in the rubrene at $V_g = 0$, and gradually get expelled as we increase the bias voltage. To trace the density of mobile holes at the rubrene surface as a function of bias voltage, we integrate $\Delta \mathrm{OD}$ over the spectral range of the broad peak. For each spectrum (i.e., each value of V_g), this integral gives a scalar that is proportional to the density of optically accessible holes, $\Delta \sigma_{IR} \propto \int \Delta \mathrm{OD}(\omega) \, d\omega$. Since we know the total amount of charge injected into the device from the concurrent electrical measurement, we can calibrate $\Delta \sigma_{IR}$ to $\Delta \sigma_E$ in the low-bias
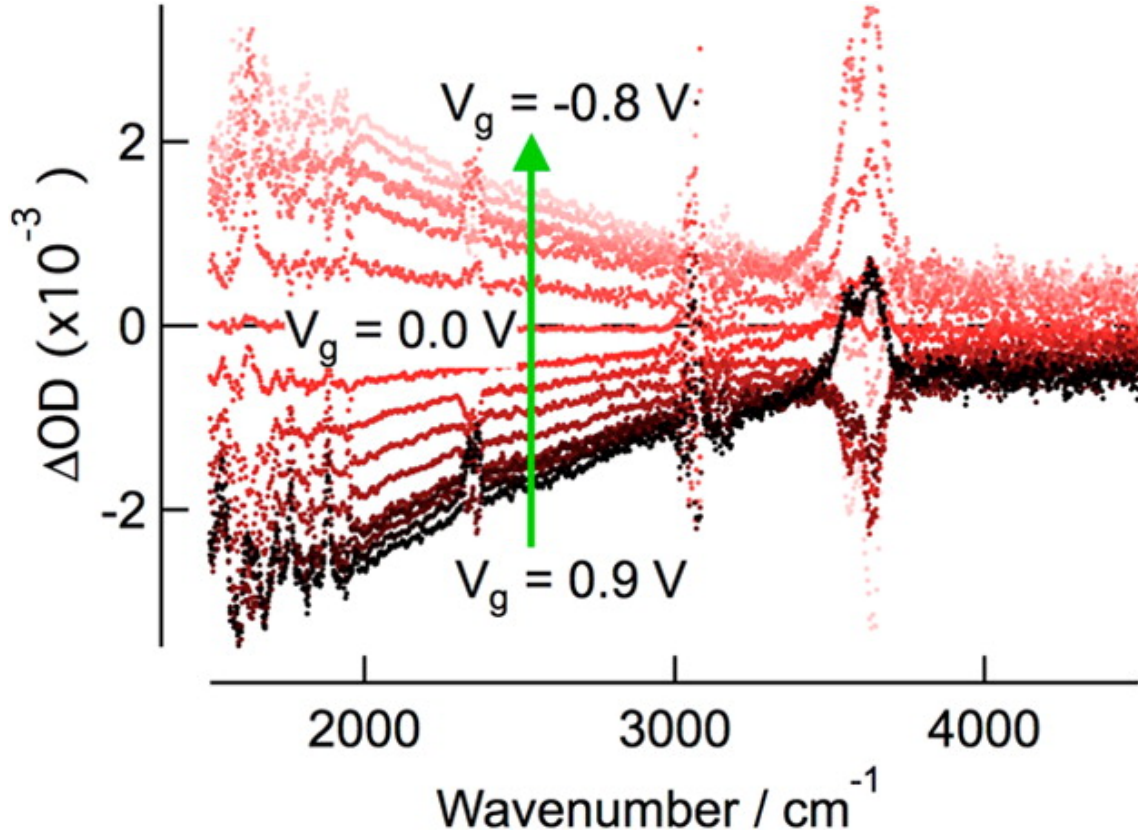
Figure 3.4: IR absorption spectrum at difference applied voltage across the rubrene capacitor, V_g: from bottom to top, $V_g = 0.9$ V to $V_g = -0.8$ V. All spectra are referenced to that at $V_g = 0$ V. The broad spectral feature, which increases with decreasing wavenumber, is assigned to free-hole absorption in crystalline rubrene. The sharp peaks on top of the broad feature are vibrational peaks of the ion-gel and rubrene. We note the presence of extraneous features at 3600 cm^{-1} (broad) and below 1600 cm^{-1} and then at 2500 cm^{-1} that correspond to atmospheric fluctuations in water and CO_2, respectively. The very low signal-to-noise ratio at just above 3000 cm^{-1} corresponds to C-H stretches in the rubrene and ion gel absorbing all of the photons of that energy range. Figure reprinted with permission from reference 58. Copyright 2015 American Chemical Society.

regime $(-0.2$ V $< V_g < 0.2$ V), where both data sets are linear in V_g. The resulting $\Delta\sigma_{IR}$ versus V_g is plotted in Figure 3.5a,b, along with the corresponding $\Delta\sigma_E$ versus V_g, for two different samples. These devices were made with different materials for the electrical contact to the IG, but nonetheless show similar results.
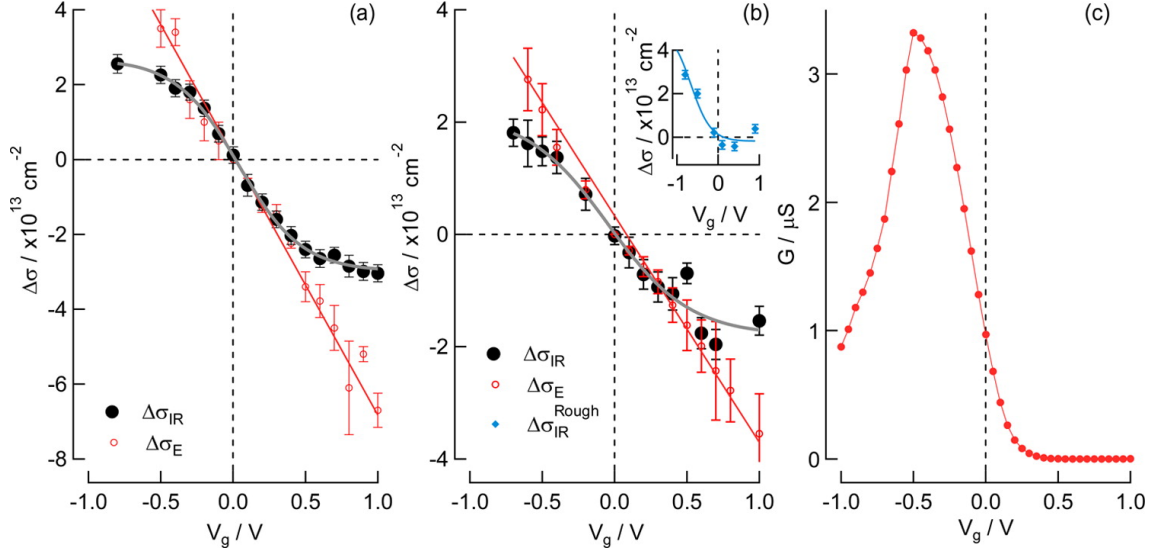
Figure 3.5: Surface charge density in rubrene, $\Delta\sigma$, as a function of gate bias, V_g for a device with (a) graphite and (b) gold contact to the ion gel. The solid black circles are derived from the spectroscopic signature of free-holes in rubrene, $\Delta\sigma_{IR}$, and the solid gray curves are sigmoidal fits as guides for the eye. The red dots are obtained from electrical charging/discharging measurements, $\Delta\sigma_E$ and are used to calibrate the spectroscopy data (SI, section 3). Error bars are the standard error of the mean determined by the averaging of charge modulation measurements. Inset in panel b shows spectroscopic $\Delta\sigma$ obtained for a device fabricated from a rough rubrene crystal, and the blue curve is a sigmoidal fit as a guide for the eye. (c) Conductance, G, defined as the drain current, $I_d(Vg)$, divided by the source-drain voltage, $V_{sd} = -0.1$ V, of a rubrene [EMIM][TFSI] gated transistor as fabricated in reference 17. The device turns on when $V_g > 0$ V due to the intrinsic doping of free charge carriers seen spectroscopically. The drop in conductance when $Vg < -0.5$ V corresponds to the saturation of free charge carriers observed in the CM spectra. Figures reprinted with permission from reference 58. Copyright 2015 American Chemical Society.

3.2   Results and Discussion

In both samples, we see $\Delta\sigma_{IR} < 0$ for $V_g > 0$ V, that is, holes getting removed from the rubrene as the bias voltage increases from zero. The depletion only saturates for $V_g > 0.9$ V, which marks the point where (nearly) all delocalized holes have been expelled from the rubrene. This corresponds to a density of $\sim 2 \times 10^{13}$ mobile holes per cm^2 present at the rubrene surface at $V_g = 0$ V.

We note that $\Delta\sigma_{IR}$ also saturates for strongly negative bias, $V_g < -0.5$ V, whereas the total amount of injected charge $\Delta\sigma_E$ (determined from the electrical data) remains linear in V_g over a wider range. The broad IR absorbance feature (Figure 3.4) through the semiconductor selectively probes the density of mobile and delocalized carriers. Thus, the

excess injection/extraction of charge beyond the saturation points in $\Delta\sigma_{IR}$ is attributed to population and depletion of more localized sites, such as deep traps or small polarons, as discussed further below.

The intrinsic (zero-bias) doping at the rubrene interface is orders of magnitude higher than any residual doping in the bare crystal, and appears upon the formation of the semiconductor/ion-gel interface. This phenomenon is also observed in transport measurement, which shows conductivity through electrolyte-gated single-crystal rubrene transistors also in the absence of applied gate voltage.[17,53] An example of such a measurement is shown in Figure 3.5c. This kind of intrinsic doping has not been observed in rubrene devices gated with conventional dielectrics (without mobile ions).[16,63,64] We conclude that there is a thermodynamic driving force for capacitive charging of the organic semiconductor/ion-gel interface. Upon forming the rubrene/ion-gel interface, the holes can latch to the surface of rubrene to stabilize the anions on the ion-gel side. This is followed by additional hole injection from the metal electrode (contacting rubrene) to reach a thermodynamic equilibrium. The opposite situation, i.e., the accumulation of electrons at the rubrene surface to stabilize cations in the electrolyte, does not occur because rubrene is predominantly a hole conductor. Holes move through rubrene with little trapping and a high mobility ($\mu_h > 1$ cm^2 V^{-1} s^{-1}), while electron mobility is low ($\mu_e < 1$ cm^2 V^{-1} s^{-1}) and is easily trapped. As such, there is a thermodynamic penalty for the electrons to detrap and reach the interface. Furthermore, injecting electrons into rubrene from the Au electrode is also unlikely due to a large energetic offset between the rubrene conduction band and the Au Fermi level.[65,66]

Support for this interpretation can be found in the work of Podzorov and co-workers who demonstrated the spontaneous accumulation of mobile holes and the healing of hole traps at the crystalline interfaces between organic semiconductors, including rubrene, and an inert polymer containing polar groups with large local dipole moment.[52] In their case, the intrinsically doped holes are stabilized by the local dipoles on the polymer chain, and

the time profile of this doping process reflects the relaxation dynamics of the polymer chain.

Further support for this intrinsic doping mechanism emerges from a comparison between devices made from optimized rubrene single crystals with smooth surfaces (Figure 3.5a,b, main panels) and crystals with rough surfaces (Figure 3.5b, inset). We obtain the latter by growing rubrene single crystals at temperatures and flow rates higher than those at optimal conditions.[67] Under these conditions, layer-by-layer growth in the rubrene a-b plane is less favorable, resulting in a rough crystalline surface topology with steps in the c-crystalline direction. The device with rough rubrene shows no intrinsic doping: the $\Delta\sigma_{IR}^{\text{Rough}}$ versus V_g curve shows an onset of injected hole density at $V_g = 0$ V. Since the hole mobility along the c-direction is much lower than that along the a-b plane and is nearly the same as electron mobility,[9] the transport of holes along the rough rubrene crystalline surface must overcome a large number of energy barriers due to steps along the c-direction. As a result, holes are now inhibited like electrons from reaching the rubrene/IG interface. Thus, an electric double layer cannot form without gate bias.

Having discussed the origin of the intrinsic doping, we now address the differences between $\Delta\sigma_E$ and $\Delta\sigma_{IR}$ for $|Vg| > 0.5$ V, as seen in figure 3.5a,b. While spectroscopic measurements reveal saturation in $\Delta\sigma_{IR}$ at both the positive and negative extremes of V_g, the electrical data indicate a linear dependence of $\Delta\sigma_E$ on V_g in the gate bias range investigated. To explain this, it is important to note that the broad IR absorbance measures mobile carriers, while the electrical measurement counts the total charge. Hence, we conclude that holes injected at $V_g < -0.5$ V occupy states that are too localized to be detected in the IR absorption. A related phenomenon is seen in measurements of electrical transport through transistor devices (Figure 3.5c), where the drain-source conductance shows a decrease under moderately to strongly negative gating. Previous publications have attributed this conductance drop to trapping by anion clusters forming at larger applied biases, a model that is consistent with our data.[17,53] In the positive saturation regime, $V_g > 0.5$ V, where

the IR spectroscopy tells us that the rubrene is depleted of mobile holes, the linear relation between V_g and $\Delta\sigma_E$ still persists. This indicates further extraction of localized holes, e.g., from deep traps, which are IR-invisible and do not contribute to transport (Figure 3.5c). Although transport measurements have generally shown the rubrene-electrolyte interface to be robust,[53] we cannot rule out electrochemical contributions to the capacitor charging current.[68]

In summary, we carry out combined spectroscopy and electrical measurements on a model electrolyte gated organic semiconductor interface: single crystal rubrene/ion-gel. We unambiguously show the presence of a high density of intrinsic doping at the organic semiconductor/ion-gel interface. We explain this intrinsic doping as resulting from a thermodynamic driving force. Spectroscopic measurements also reveal the saturation of free-hole like carrier density at the rubrene/ion-gel interface at $V_g < -0.5$ V, which is commensurate with the negative transconductance seen in transistor measurements.

Chapter 4

Defects in Monolayer MoS$_2$

As mentioned previously, one major limitation to the viability of MoS$_2$ as a commercial material is the prevalence of defects within the material.[69–71] Also, this limits our ability to study its intrinsic properties as a 2D semiconductor. Hence, devices typically have room temperature mobilities on the order of hundreds cm^{2}V^{-1}s^{-1}[39] and PL quantum yields on the of only ~ 0.1 %.[72] Mid-gap states which serve as trapping and scattering sites (i.e. τ in equation 1.7 becomes short) for moving charges and excitons are prevalent in MoS$_2$.
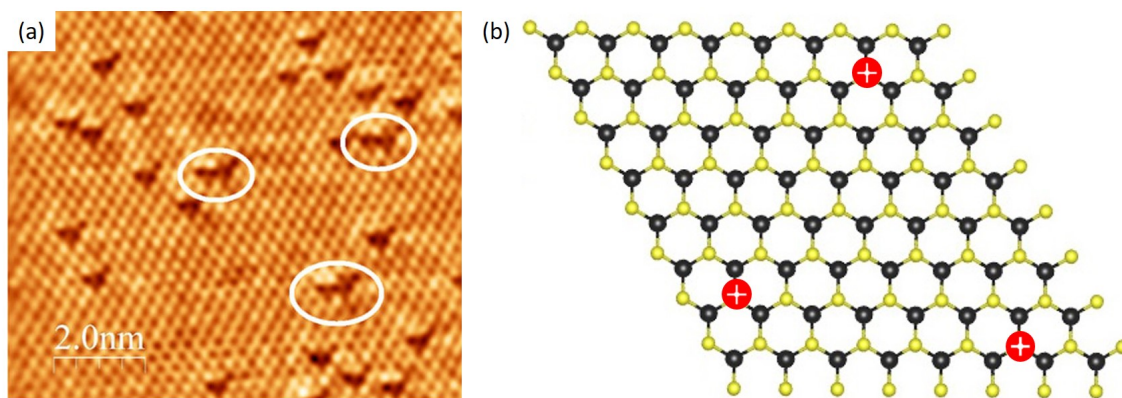
Figure 4.1: (a) An STM image of a MoS$_2$ surface showing sulphur missing in the lattice, the white circles emphasizing a few sites. Figure adapted from reference 71 under the Creative Commons Attribution 4.0 International License. (b) A schematic showing sulfur (yellow spheres) vacancies in MoS$_2$, the sulfur site replaced by positive charges. Molybdenum is represented by black spheres.

4.1　Sulfur Vacancies

4.1.1　n-Type Doping

A major source of defects in MoS_2 is known to the be the sulfur vacancies. During the growth of the material it's not uncommon for sulfur sites to not be completely filled. This is clearly observed in the scanning tunneling microscopy of the monolayer MoS_2 shown figure 4.1 (a).[71]

Removing the sulfurs monolayer lattice results in dangling bonds on the molybdenum and locally positive charged sites. The Mo^{4+} is no longer completely charge balanced with two S^{2-}s which causes this local positive charge (illustrated in figure 4.1 (b)).[71,73] The electrons from the Mo dangling bonds without a sulfur to bond with are capable of being thermally excited to the CB being in a shallow electron trap state. This raises the MoS_2 Fermi energy closer to the conduction band making the MoS_2 typically intrinsically an n-doped material. This can be seen in MoS_2 FET transfer curves in figure 1.13 (b) in which the threshold voltage is dramatically shifted to the negative voltages, showing that even ungated MoS_2 has conductive electrons.[39]

Trion Quasiparticle

This excess electron density results in a rather special many-body effect within MoS_2 optical properties: namely the formation of the trion species. A trion illustrated in figure 4.2 (b) is a quasiparticle made up of an exciton interacting with an additional charge, in the case of MoS_2, an electron.[34,74] Typically, the charge density required to observe such a species is extremely high; however, since monolayer MoS_2 is a 2D semiconductor the excess electrons are only located on the 2D plane so the excitons formed after an optical excitation will encounter a very high density of excess electrons, instead of diffusing freely in the bulk.

The PL from the trion quasiparticle (labeled as A^- in figure figure 4.2 (a)) is slightly red shifted from the excitonic PL due to the additional binding energy of the three particle interaction (instead of just the two particle excitonic interaction). The presence of the trion within the PL is indicative of a rather defective MoS_2 sample with many sulfur vacancies and excess electrons. This results in MoS_2 samples with very low PL quantum yields (i.e. very dim PL) since there are many non-radiative recombination channels.
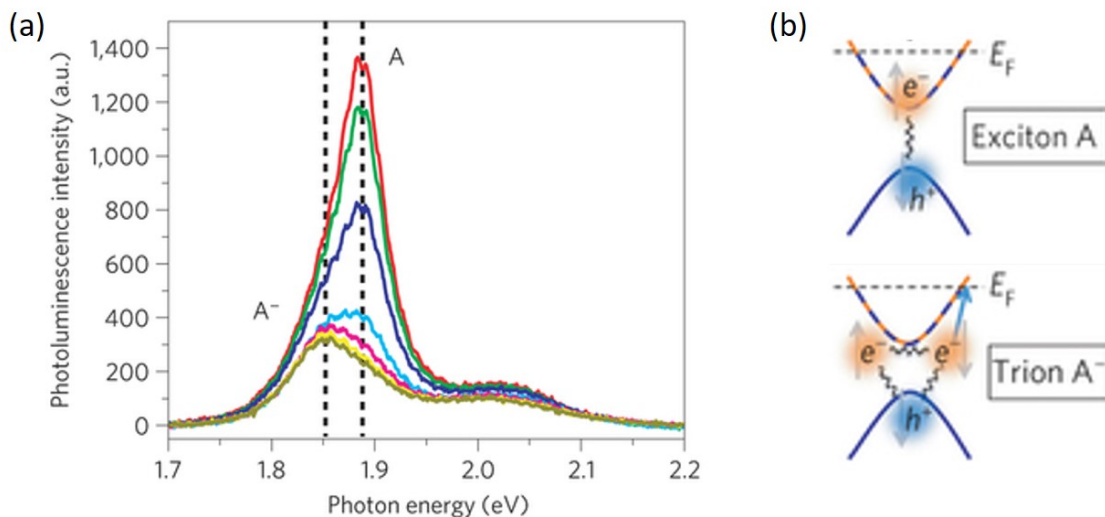
Figure 4.2: Figures adapted from reference 34 (a) A PL spectrum when the MoS_2 is gated at different voltages. There is a blue shift and a brightening of the PL as spectrum moves from being dominated by the trion, A^-, peak to the excition, A, peak due to the removal of electrons by the gating voltage. (b) shows an illustration of top: an A exciton, showing strong interaction between the electron and the hole and bottom: an A^- trion with two electrons and a hole and resulting in an increased binding energy in comparison to the exciton.

4.2   Uncharged Defects

Another major source of defects that hamper device performance are the uncharged defects.[75] These types of defects have haunted the semiconductor community since it's inception as they are ubiquitous and can be difficult to characterize. In the case of MoS_2 these can be a result of wrinkles or bubbles in the monolayer or local stretching/compression in the lattice altering the band structure creating local minima.[76] Another possible uncharged defect is an atomic substitution within the lattice, such as a oxygen atom (also a chalcogenide

with a common oxidation state of -2) replacing or filling a vacant sulfur site hence remaining neutral but potentially leaving a mid-gap state.[77–79] Finally, since monolayer MoS_2 is effectively entirely an interface, it is subject to any structural or electrostatic inhomogeneity from its substrate strongly modulating its electronic properties.

4.3   Defect Mitigation Methods Through Surface/Interface Treatment

Hence, in order to make the material more functional in electrical devices and access MoS_2's intrinsic properties, many strategies have been employed to limit the effects traps by chemically treating the interface or protecting it. In the following section I go through a few illustrating the key points in what is required for treating monolayer MoS_2.

4.3.1   Hexagonal Boronitride Encapsulation

One of the most common methods used to protect monolayer TMDCs is by encapsulation in hexagonal boronitride (hBN). hBN also being a layered Van der Waals material, but an insulator meshes well with the 2D paradigm as it can be easily exfoliated on to MoS_2 monolayer. Hence, by placing a monolayer of MoS_2 sandwiched (illustrated in 4.3 (a)) between hBN the MoS_2 PL and transport[81] properties have been shown to improve dramatically. The monolayer is no longer in contact with the heterogeneous SiO_2 and compressed between the hBN forcing it to keep a flat structure. Figure 4.3 (b) shows the reflectivity and the PL at $T = 4$ K showing a sharp line width, suppression of trap PL and a much higher quantum yield.[80,82]
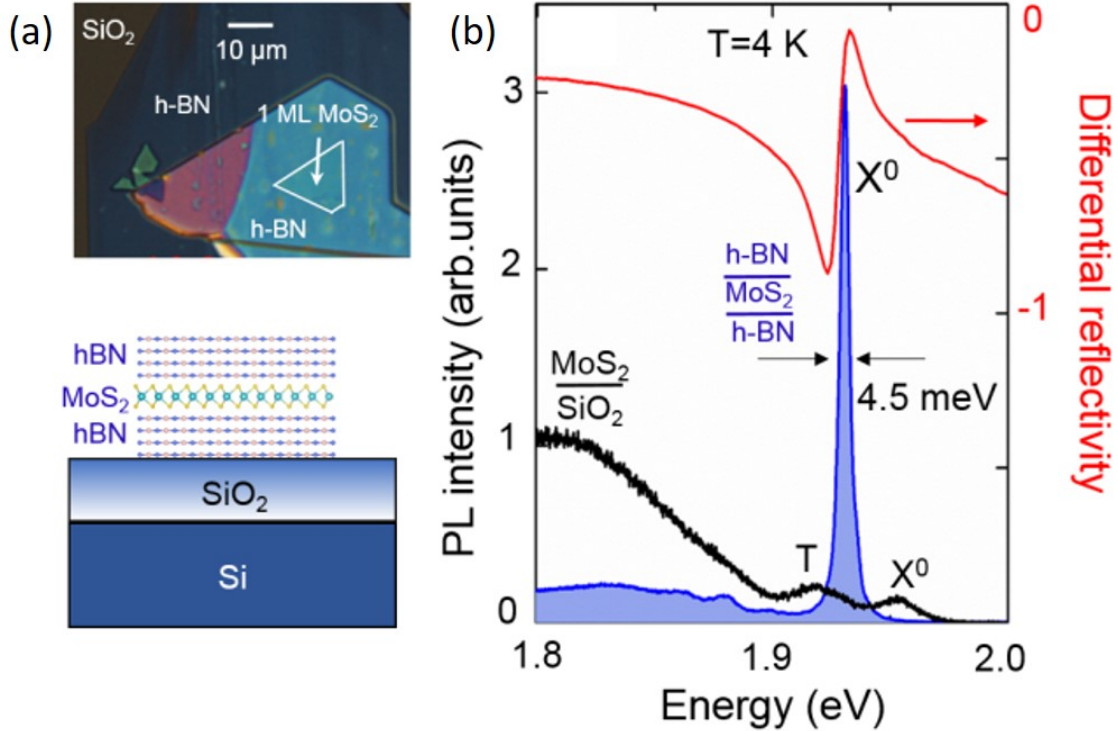
Figure 4.3: (a) Top: an optical microscope image of a hBN encapsulate MoS$_2$ monolayer on a SiO$_2$ substrate. Bottom: an illustration of the cross-section of the hBN encapsulated MoS$_2$ sample. (b) The PL spectrum of encapsulated MoS$_2$ (blue) and bare MoS$_2$ (black) on SiO$_2$ at 4 K as well as the reflectivity of the encapsulated MoS$_2$ (red). Encapsulation results in negligible homogeneous broadening and much brighter excitonic PL intensity while diminished broad low energy trap emission implying a much higher sample quality. Figures adapted from reference 80.

4.3.2 Self-Assembled Monolayers

Another method to deal with the substrate inhomogeneity is to grow a self-assembled monolayer (SAM) on the substrate. By placing on SiO$_2$ a monolayer of organic molecules with fatty tails the monolayer TMDC is protected. Figure 4.4 shows the comparison of the PL of MoSe$_2$ when placed on a SiO$_2$ substrate without a SAM (a) and with a SAM (b): the trion peak was suppressed significantly and the homogeneous linewidth the of the peak also narrowed.[82]

44
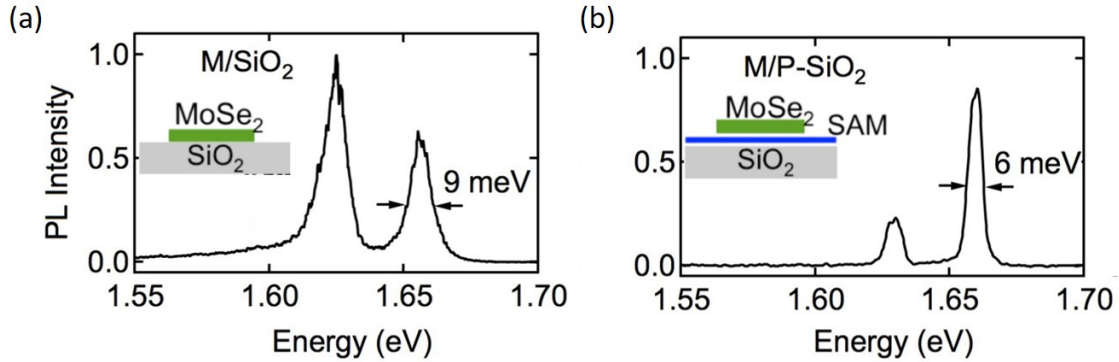
Figure 4.4: (a) 4 K PL spectrum of bare MoSe$_2$ on SiO$_2$ and (b) MoSe$_2$ with a SAM covered SiO$_2$. Sample quality has improved showing narrower peaks and a suppression of the trion emission. Figures reproduced from reference 82 by permission of IOP Publishing. All rights reserved.

4.3.3 Oxygen Treatment

One method developed to deal with the sulfur vacancies in MoS$_2$ is that of treating the monolayer with oxygen. Figure 4.5(a) shows how an O$_2$ molecule may sit favorably at a sulfur vacancy site with an effective hole transfer to the O$_2$ stabilizing the site and potentially screen the positive charge. Figure 4.5(b) shows how the PL intensity increases as a result of employing an oxygen plasma as well as a blue shift to the excitonic peak location away from the trion species.[73]
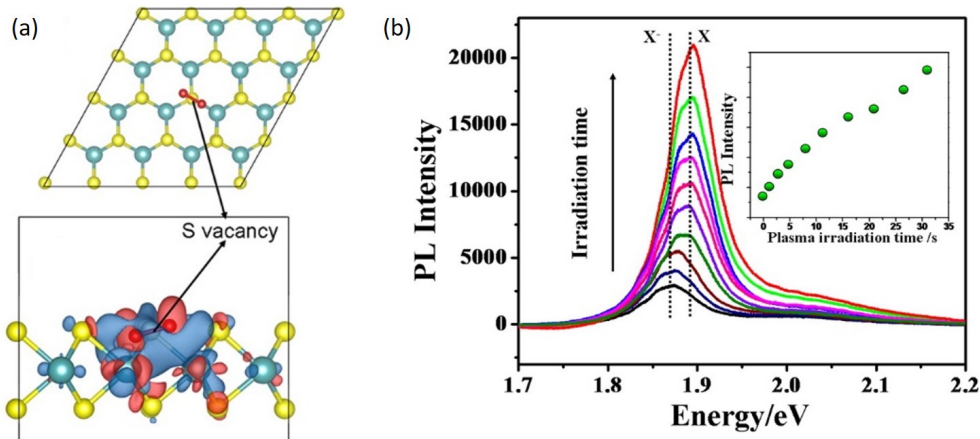
Figure 4.5: (a) Top: a schematic of an O$_2$ molecule sitting a sulfur vacancy site, bottom: (b) a close up of the chemisorption of the O$_2$ molecule at the sulphure vacancy and the localization of the hole wavefunction on the O$_2$. The enhanced PL spectra of MoS$_2$ as function of O$_2$ plasma irradiation time showing a brightening and blue shift corresponding to the quenching of the trion, meaning removal of excess electrons. Figures reprinted with permission from reference 73. Copyright 2016 American Chemical Society.

4.3.4 Super Acid Treatment

Work by Amani *et al.* shows that by rinsing an exfoliated monolayer MoS_2 they were able to increase the PL quantum yield from $\leq 1 \%$ to almost 100 %.[72,83] This over two orders of magnitude increase is shown by the images in figure 4.6.
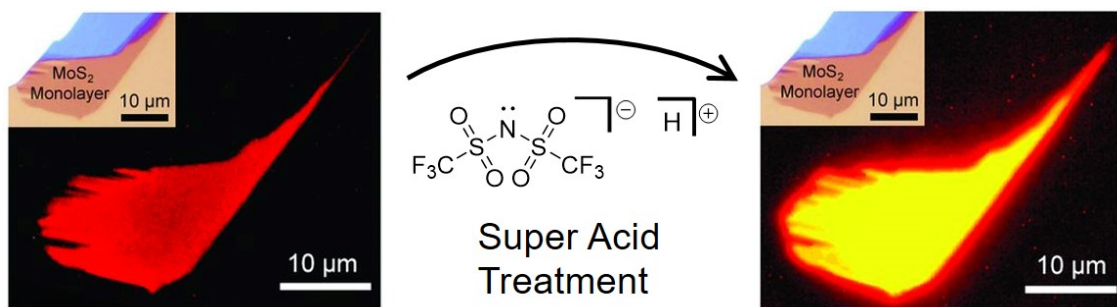
Figure 4.6: Figures showing the PL image of monolayer MoS_2 before and after treatment with the H[TFSI] superacid resulting in over two orders of magnitude enhancement of PL - brightening the image significantly. Adapted from 72. Reprinted with permission from AAAS.

What is of interest in the use of the super acid is that the anion component, bis(trifluoro-methylsulfonyl)amide [TFSI], is also a common anion in an IL.[17] Hence, what seems to be happening is that anions are localizing on the positively charged sulfur vacancies and passivating them. Furthermore, the protons in the super acid is likely then reduced by the MoS_2 to evolve H_2 gas, a process known to occur in highly defective MoS_2 with lots of sulfur vacancies (illustrated in figure 4.7).[84]

Figure 4.7: Schematic of the catalytic reduction of protons by the sulfur vacancies in MoS_2. Figures reprinted with permission from reference 84. Copyright 2016 American Chemical Society.

A general mechanism of treating charged defects at interfaces through electrostatic screening

needs to be explored to confirm this hypothesis.

Chapter 5

Electrostatic Screening of Charged Defects in Monolayer MoS$_2$

[85] As mentioned previously monolayer transition-metal dichalcogenides (TMDCs)[30,31] show promise as model systems for two-dimensional (2D) physics and for nanoscale electronic, optoelectronic, and photonic devices.[35,40,42,43,86–88] However, the prevalence of defects[69–71] that serve as uncontrolled dopants, charge carrier traps, and non-radiative recombination centers stand as a major barrier to studying intrinsic 2D physics and for the realization of efficient monolayer devices.[89–92] While optimizing the growth process of 2D materials reduces atomic defects, other defects may form as a result of exfoliation, device fabrication, and chemical/thermal damage. Furthermore, a monolayer TMDC effectively functions as an interface making its electronic properties highly sensitive to its local environment, such as chemical, topological, and electrostatic inhomogeneity on the supporting substrate surface. Several strategies have been employed to mitigate or reduce traps in TMDC monolayers, including super-acid treatments,[72,83,93] molecular oxygen adsorption,[73] substrate selection or passivation,[94] and encapsulation in hexagonal boron nitride.[81,82,95] Here we demonstrate a simple and reversible approach to reduce nonradiative trap centers in monolayer MoS$_2$.

48
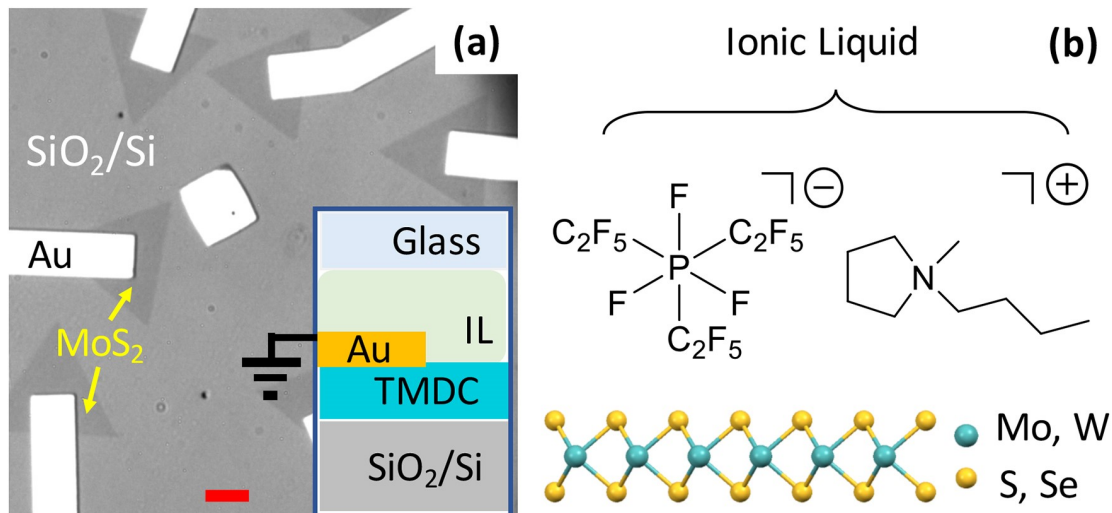
Figure 5.1: (a) Optical microscope image of CVD MoS_2 flakes (dark triangles) with Au metal contacts (bright strips) on a SiO_2/Si substrate. Scale bar (red): 10 μm. The inset shows schematically the sample after contact with an ionic liquid; (b) Molecular formula of the ionic liquid and atomic model for a TMDC monolayer. Figures reprinted with permission from reference 85. Copyright 2017 American Chemical Society.

We find that charged defects in MoS_2 monolayers can be electrostatically passivated by contact with ionic liquids (ILs). ILs are extensively used as gate dielectrics because the high capacitance from the interfactial electric double layer formation enables very high charge injection densities ($> 10^{14}$ cm^{-2}) at low gating voltages.[1,20,96] Notably, high density doping from IL gating has led to the demonstration of superconductivity in TMDCs.[49–51] However, electrostatic interaction also spontaneously occurs between the mobile ions in an IL and charges on a semiconductor surface.[58] Here we show that such interactions can reduce doping and increase photoluminescence (PL) intensity by up to two orders of magnitude in TMDC monolayers. We interpret these findings as the screening of charged trap sites in the TMDC monolayer by mobile anions in the IL, an effect which is similar to the "healing" of surface defects on organic semiconductors by local polar bonds in perfluoropolyether (PFPE).[52]

5.1   IL/Monolayer MoS$_2$ MIS Capacitor Fabrication

The samples used in the present study consist of monolayers of MoS$_2$ from chemical vapor depositions (CVD) or exfoliation. Typically, we chose monolayer TMDC flakes with lateral dimensions of $\sim 10~\mu$m either grown or exfoliated onto SiO$_2$/Si substrates. Through e-beam lithography we introduced Ti/Al/Au contacts (see optical microscope image in figure 5.1a). For larger samples we painted graphite (TEDPELLA) electrodes onto the MoS$_2$ flakes. To form the TMDC/IL interface, we deposited a small drop of an IL on the sample and then covered the sample with a glass coverslip. We performed all PL measurements at room temperature in a dry N$_2$ atmosphere or in vacuum on a home-built epi-fluorescence microscope, with the excitation light from CW lasers emitting 532 nm or 514 nm and at power densities of 4 kW·cm^{-2}. We measured PL far ($> 1~\mu$m) from the electrodes to avoid quenching by the Au/graphite.

5.2   IL/Monolayer MoS$_2$ MIS Capacitor Photoluminescence Microspectroscopy

We carried out photoluminescence measurements using home-built far-field epi-fluorescence microscope set-ups (Olympus IX73 or Nikon TE300 inverted microscopes). We mounted all samples in either a N$_2$-gas-filled cell or evacuated cryostat for optical measurements. The excitation light used was either a 532 nm commercial frequency doubled YAG laser (MDL-III-532-200mW) or an Argon ion laser operating at 514.5 nm (CVI Melles-Griot). The light was focused onto the sample surface by a 40×, NA 0.60 objective with a correction collar (Olympus LUCPLFLN40X or Nikon CFISPLFLELWD40X). The laser spot size was focused to spot size of 0.7 μm diameter. The emission from each monolayer was collected by the same objective and focused into a spectrograph (Princeton Instrument

Acton SP2300i with a 300 mm^{-1} grating or Princeton Instruments Acton 300i with a 150 mm^{-1} grating) and detected by a CCD camera (charge-coupled device; PyLoN 400 or PI-Photon). The instrument resolution was ~ 0.4 nm. All measurements were carried out at room temperature.

5.3   Results and Discussion

The PL yield from MoS$_2$ monolayers are known to be low, typically $< 1\%$, and vary greatly depending on sample preparation.[30,31,72,94] figure 5.2 shows representative PL spectra (dashed curves) from different monolayer MoS$_2$ flakes on the SiO$_2$ surface. We find that the PL intensity from these CVD samples vary by as much as one-order of magnitude from sample to sample (dashed curves in figure 5.2a-c). Each PL spectrum features a main exciton peak at 1.89 eV and a lower energy shoulder at ~ 1.85 eV which is attributed to trions.[34] After applying an IL to each monolayer MoS$_2$ flake, we find that the PL intensity from the exciton peak for each spectrum (solid curves in figures 5.2a, 5.2b or 5.2c) increases by one to two orders of magnitude while the trion peak is no longer resolved relative to the dominant exciton peak. Within experimental uncertainty, there is little change to the exciton peak position before and after contact with IL. The removal of electrons from the MoS$_2$ monolayer has been shown to induce a small red-shift in the exciton PL peak,[34] while the increased dielectric screening by IL is expected to induce a blue-shift.[97] For the sample in figure 5.2d, the apparent "blue" shift with IL simply results from the fact that the lower-energy trion emission dominates before IL contact, while the exciton emission dominates after IL.

The PL enhancement effect requires a grounded metal contact to the TMDC monolayer. As shown in figure 5.2d for one CVD MoS$_2$ flake, in the absence of a metal contact, the PL increases only slightly ($\sim 40\%$) upon contact with an IL (red dashed $\rightarrow$ red solid curve), while the same sample shows an order of magnitude increase in PL intensity when grounded
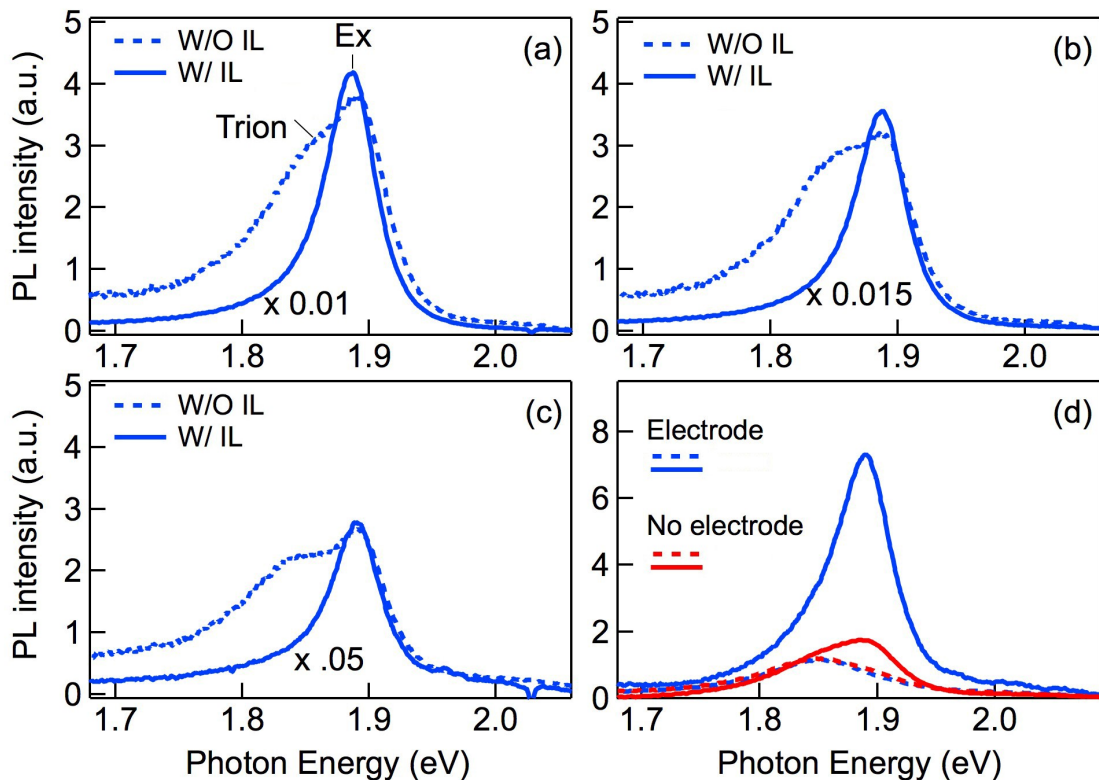
Figure 5.2: Photoluminescence (PL) spectra from MoS_2 monolayers in the absence (dashed) and presence (solid) of an ionic liquid for three different samples (a-c). Note the different scaling factors for the solid curves: (a) x 0.01, (b) x 0.015, and (c) x 0.05. (d) PL spectra from two monolayer MoS_2 flakes on the same sample, one with (blue) and one without (red) Au electrode contact. The dashed and solid curves represent the absence and presence, respectively, of ionic liquids. Figures reprinted with permission from reference 85. Copyright 2017 American Chemical Society.

(blue dashed → blue solid curve). As we discuss in detail below, the necessity of electrical grounding for the enhancement of PL intensity is consistent with the electrostatic screening of charged defects by the high dielectric environment of an IL.

We quantitatively establish the correlation between the enhancement factor (γ) in PL intensity (by IL) and the brightness of the sample for the CVD MoS_2 monolayer samples, such as those in figure 5.2. Here, we define γ as the ratio of the PL intensity in the presence and absence of an ionic liquid. figure 5.3 plots γ versus the PL intensity in the absence of an ionic liquid, I_{ex}^0, from the CVD MoS_2 monolayer samples investigated here. The enhancement factor, γ, rises monotonically with I_{ex}^0. The data point near the origin (triangle) is the average value of measurements from a dim sample with pre-treated PL intensity approximately two-
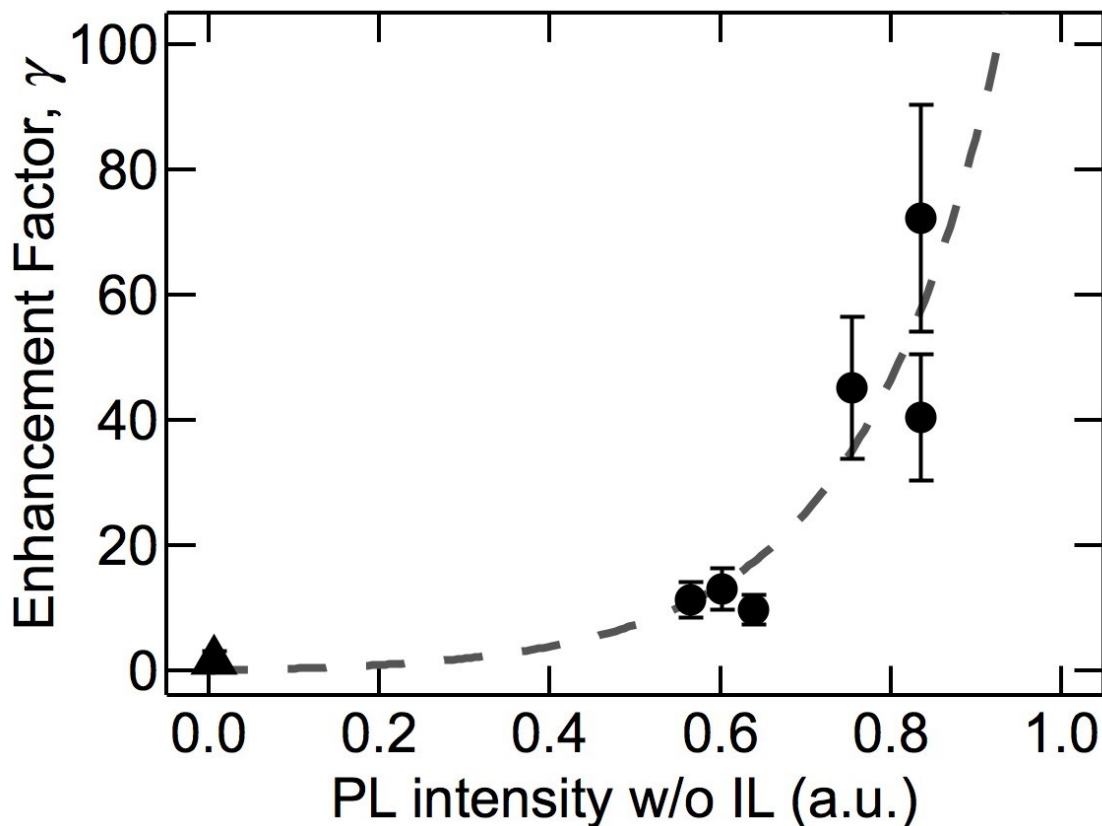
Figure 5.3: The enhancement factor (γ)in exciton intensity by the presence of an ionic liquid as a function of the original exciton PL intensity (I_{ex}^0) of MoS_2 monolayers. The solid circles are data points and the dashed line is an exponential fit which serves as a guide to the eye. Figure reprinted with permission from reference 85. Copyright 2017 American Chemical Society.

orders of magnitude lower than those from the bright samples (circles); the enhancement factor from this dim sample was $\gamma \approx 1.5$.

We test the reversibility of the PL enhancement effect by rinsing off and re-applying the IL. As shown in figure 5.4 for a monolayer MoS_2 flake with Au electrode contact, the PL spectrum (blue dashed curve) initially shows low intensity, then is enhanced with the addition of IL (blue solid curve). The PL intensity is reset to the initial level when we rinse off the IL (red dashed curve) and is enhanced again when we reapply an IL to the MoS_2 monolayer (red solid curve). Within experimental uncertainty ($\pm 20\%$) in PL intensity from measurement to measurement, we conclude that the enhancement of the PL intensity by an IL is reversible.
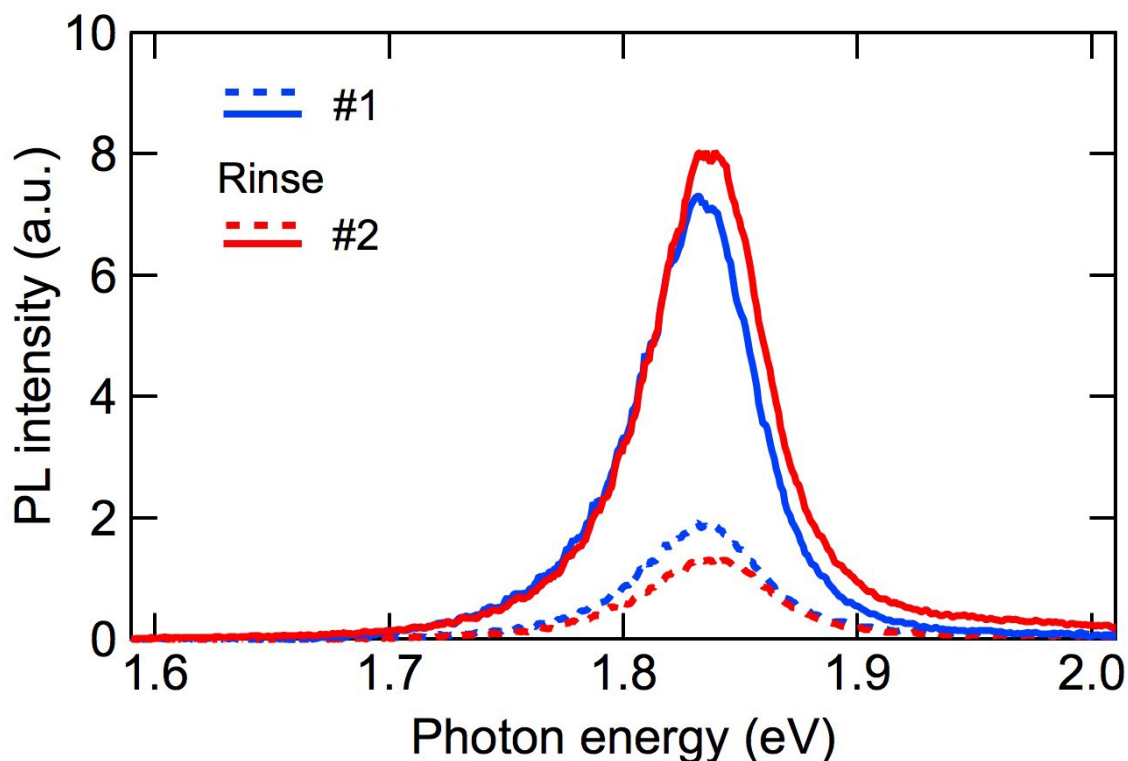
Figure 5.4: Reversible effect of PL enhancement from a CVD MoS_2 monolayer flake with an Au electrode contact. The blue spectra are from MoS_2 monolayers in the absence (dashed) and presence (solid) of an ionic liquid. The red spectra show the PL spectra after removing the IL (dashed) and reapplying the IL (solid). Figures reprinted with permission from reference 85. Copyright 2017 American Chemical Society.

The observed enhancement of the PL intensity by an IL and the reversibility of this effect suggest an electrostatic origin, distinct from irreversible chemical treatments. Among a number of defects identified in monolayer MoS_2, the dominant kind is the S-vacancy, which may lead to n-type doping and a positively charged site.[69–71] The latter is shown in figure 5.5a as a localized positive charge (red) with a delocalized electron (blue) in the MoS_2 monolayer (green). Upon treatment, the IL screens the localized charges, as schematically represented by the binding of anions in the IL to the trapped positive charge in MoS_2. The chemical potential of the electron in the MoS_2 monolayer is increased by such screening and this leads to a depletion of electrons (i.e., majority carrier from n-type doping) from the conduction band (figure 5.5b) into ground. This is consistent with the disappearance of the trion peak in PL spectra after the MoS_2 monolayer contacts the IL and the need of electrode contact (figure 5.2). Both positively-charged and neutral traps located within the bandgap can serve

as non-radiative recombination centers via Auger-type of mechanisms, as proposed by Wang *et al.*[91] The positively-charged traps can be reversibly passivated by ionic liquids, leading to the enhancement in PL yield, but the charge-neutral traps cannot. Examples of charge-neutral traps may include anti-sites and O-S substitutions.[77–79,98] The co-existence of both neutral and charged traps for non-radiative recombination can explain the observed strong correlation between γ and I_{ex}^0 as seen in figure 5.3. The concentrations of both types of traps are likely correlated, i.e., both increase with increasing defect density. Since electrostatic passivation by an IL only passivates the charged traps, the enhancement factor correlates inversely with the neutral trap density or total defect density. This is responsible for the positive correlation of γ with I_{ex}^0, figure 5.3.

The observed PL enhancement by an IL and the proposed electrostatic passivation mechanism are consistent with previous reports of PL enhancement in MoS_2 monolayer by oxygen adsorption or super-acid treatment. Nan *et al.* reported PL intensity enhancement by as large as 10^3 when defective MoS_2 monolayers were treated with oxygen and suggested that the adsorption of oxygen to S-vacancy sites is responsible.[73] Since the chemisorbed oxygen atoms/molecules should be in a partially reduced state (negatively charged), there can be an electrostatic contribution to the passivation of positively charged traps. Javey and coworkers reported the enhancement in PL efficiency to as large as unity when MoS_2 monolayers were treated with a superacid, bis(trifluoromethane) sulfonimide (TFSI).[72,83,93] TFSI is a common anion in ionic liquids. We posit that the reduction of TFSI by electrons in the n-type MoS_2 leads to hydrogen (gas) evolution, resulting in TFSI anions that passivate positively charged defects/traps. In fact, several studies show that S-vacancies provide active sites in MoS_2 catalysts to evolve hydrogen gas.[84,99,100]

In summary, we demonstrate the effective screening and passivation of charged defects in monolayer MoS_2, leading to an increase in the photoluminescence yield by up to two-orders of magnitude. We show a correlation between the enhancement of photoluminescence yield
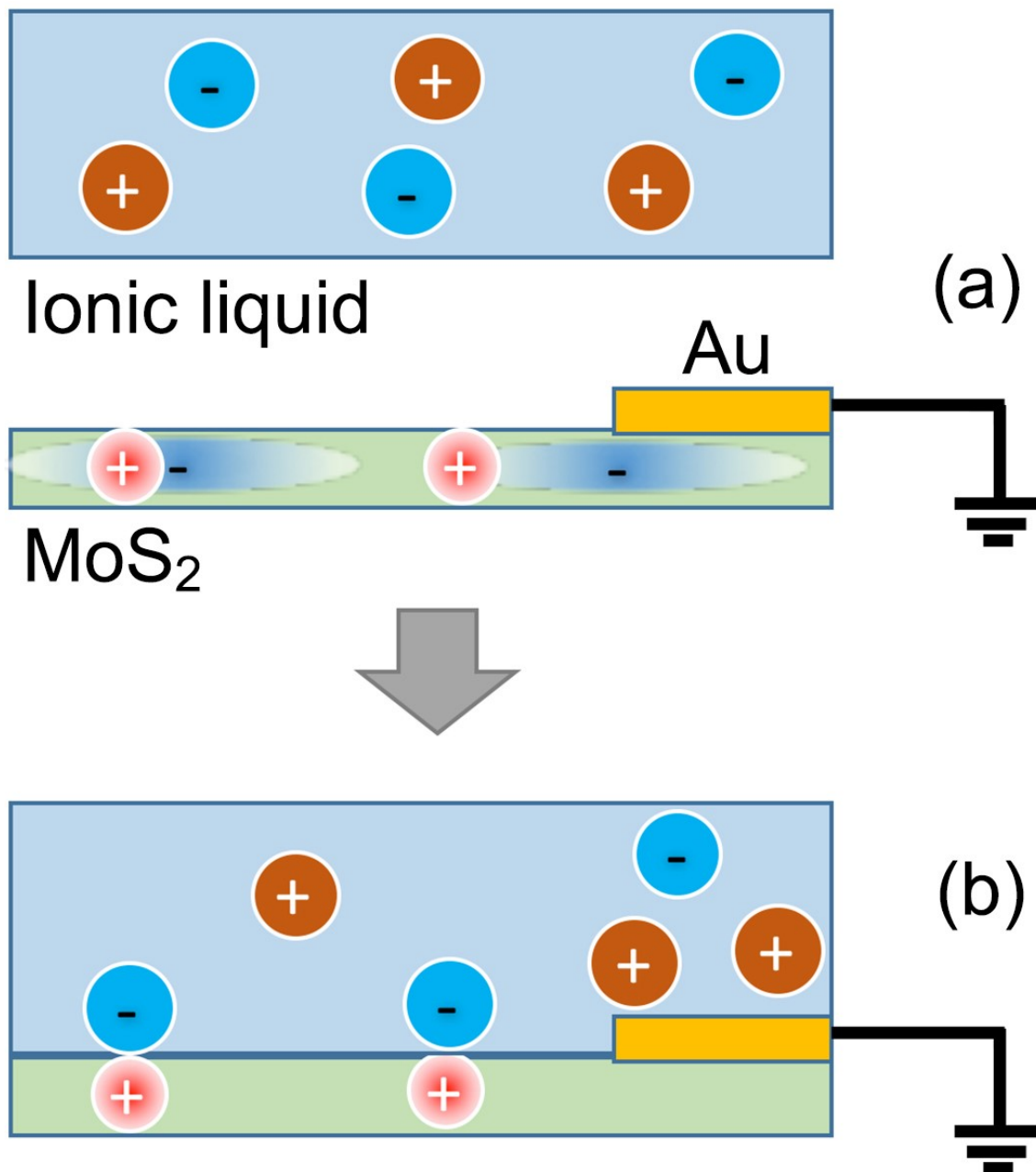
Figure 5.5: Schematic illustration of the electrostatic passivation of positively charged defects in MoS_2 monolayer (green) when it is contacted with an IL (blue). (a) Initially, the grounded MoS_2 monolayer is not in contact with the IL and so has local sulfur vacancies (shown by +) resulting in n-type doping with delocalized electrons (shown by −). (b) After contacting with an IL, the anions screen the positive charge traps and the excess electrons in MoS_2 move to the ground. Figures reprinted with permission from reference 85. Copyright 2017 American Chemical Society.

with the brightness of the MoS_2 monolayer sample and suggest the presence of both charged and neutral non-radiative recombination centers. The former can be passivated by ionic liquid, but the latter cannot. Electrostatic screening can be used as a means to passivate

charged defects, as well as to distinguish the nature of non-radiative recombination centers in monolayer TMDCs.

Chapter 6

Conclusion

Spectroscopy is a powerful method to uncover the underlying electronic properties in semiconductor materials relevant for device application and complements well the electrical transport measurements to understand the underlying physical species at dielectric/semiconductor interfaces:

In the case of the ionic liquid/rubrene interface we see that ionic liquid can passively hole dope the rubrene due to the high hole mobility relative to the electron mobility in rubrene and that even though the electrical measurements show increasing hole injection into the rubrene surface, the IR spectroscopy shows there is a saturation of mobile charge carriers in the surface which is responsible for the lowering of mobility even though the charge density ostensibly increases.

In the case of the ionic liquid/MoS$_2$ interface PL spectroscopy reveals that there is an enhancement in the PL intensity as result of the ionic liquid as well as a suppression in the trion emission due to the electrostatic screening of the positive sulfur sites using the IL dielectric, without even applying a voltage.

The ionic liquid/semiconductor interface while useful for devices in order to achieve high charge densities within the semiconductor also show effects without any applied volt-

ages due to the interacts of the ionic liquid with the electrical species at the interface of semiconductors. It is important to consider these effects when employing an ionic liquid as gating dielectric as it may not function as a conventional dielectric like SiO_2 as a result. Though these effects may not be detrimental as shown in the case of MoS_2.

Bibliography

[1] Cho, J. H.; Lee, J.; Xia, Y.; Kim, B.; He, Y.; Renn, M. J.; Lodge, T. P.; Frisbie, C. D. *Nat. Mater.* **2008**, *7*, 900–6.

[2] Sirringhaus, H.; Brown, P. J.; Friend, R. H.; Nielsen, M. M.; Bechgaard, K.; Langeveld-Voss, B. M. W.; Spiering, A. J. H.; Janssen, R. A. J.; Meijer, E. W.; Herwig, P.; de Leeuw, D. M. *Nature* **1999**, *401*, 685–688.

[3] Sakanoue, T.; Sirringhaus, H. *Nat. Mater.* **2010**, *9*, 736–740.

[4] Emin, D. *Polarons*; Cambridge University Press: Cambridge, 2013.

[5] Pope, M.; Swenberg, C. E. *Electronic processes in organic crystals and polymers*, 2nd ed.; Oxford University Press, 1999.

[6] Sundar, V. C.; Zaumseil, J.; Podzorov, V.; Menard, E.; Willett, R. L.; Someya, T.; Gershenson, M. E.; Rogers, J. A. *Science* **2004**, *303*, 1644–6.

[7] Podzorov, V.; Menard, E.; Borissov, A.; Kiryukhin, V.; Rogers, J. A.; Gershenson, M. E. *Phys. Rev. Lett.* **2004**, *93*, 086602.

[8] Sutton, C.; Marshall, M. S.; Sherrill, C. D.; Risko, C.; Brédas, J.-L. *J. Am. Chem. Soc.* **2015**, *137*, 8775–8782.

[9] Pundsack, T. J.; Haugen, N. O.; Johnstone, L. R.; Daniel Frisbie, C.; Lidberg, R. L. *Appl. Phys. Lett.* **2015**, *106*, 113301.

[10] Laudise, R.; Kloc, C.; Simpkins, P.; Siegrist, T. *J. Cryst. Growth* **1998**, *187*, 449–454.

[11] Neamen, D. A. *Semiconductor physics and devices : basic principles*, 4th ed.; McGraw-Hill, 2012.

[12] Griffiths, D. J. D. J. *Introduction to electrodynamics*, 3rd ed.; Prentice Hall, 1999.

[13] Muller, R. S.; Kamins, T. I.; Chan, M. *Device Electronics for Integrated Circuits*; John Wiley & Sons, 2003.

[14] Yu, P. Y.; Cardona, M. *Fundamentals of Semiconductors : Physics and Materials Properties*, 4th ed.; Springer, 2010.

[15] Sai, N.; Li, Z.; Martin, M.; Basov, D.; Di Ventra, M. *Phys. Rev. B* **2007**, *75*, 045307.

[16] Menard, E.; Podzorov, V.; Hur, S.-H.; Gaur, A.; Gershenson, M. E.; Rogers, J. A. *Adv. Mat.* **2004**, *16*, 2097–2101.

[17] Xia, Y.; Xie, W.; Ruden, P. P.; Frisbie, C. D. *Phys. Rev. Lett.* **2010**, *105*, 036802.

[18] Yuan, H.; Shimotani, H.; Tsukazaki, A.; Ohtomo, A.; Kawasaki, M.; Iwasa, Y. *Adv. Func. Mater.* **2009**, *19*, 1046–1053.

[19] Dhoot, A.; Israel, C.; Moya, X.; Mathur, N.; Friend, R. *Phys. Rev. Lett.* **2009**, *102*, 136402.

[20] Ueno, K.; Nakamura, S.; Shimotani, H.; Ohtomo, A.; Kimura, N.; Nojima, T.; Aoki, H.; Iwasa, Y.; Kawasaki, M. *Nat. Mater.* **2008**, *7*, 855–8.

[21] Ye, J. T.; Inoue, S.; Kobayashi, K.; Kasahara, Y.; Yuan, H. T.; Shimotani, H.; Iwasa, Y. *Nat. Mater.* **2010**, *9*, 125–8.

[22] *Organic Electronics II: More Materials and Applications*; John Wiley & Sons, 2012; p 440.

[23] Kim, S. H.; Hong, K.; Xie, W.; Lee, K. H.; Zhang, S.; Lodge, T. P.; Frisbie, C. D. *Adv. Mater.* **2013**, *25*, 1822–46.

[24] Hong, K.; Kim, Y. H.; Kim, S. H.; Xie, W.; Xu, W. D.; Kim, C. H.; Frisbie, C. D. *Adv. Mater.* **2014**, *26*, 7032–7037.

[25] Fujimoto, T.; Awaga, K. *Phys. Chem. Chem. Phys.* **2013**, *15*, 8983–9006.

[26] Kaake, L. G.; Paulsen, B. D.; Frisbie, C. D.; Zhu, X.-Y. *J. Phys. Chem. Lett.* **2010**, *1*, 862–867.

[27] Lee, J.; Kaake, L. G.; Cho, J. H.; Zhu, X.-Y.; Lodge, T. P.; Frisbie, C. D. *J. Phys. Chem. C* **2009**, *113*, 8972–8981.

[28] Kaake, L. G.; Zou, Y.; Panzer, M. J.; Frisbie, C. D.; Zhu, X.-Y. *J. Am. Chem. Soc.* **2007**, *129*, 7824–30.

[29] van der Zande, A. M.; Huang, P. Y.; Chenet, D. A.; Berkelbach, T. C.; You, Y.; Lee, G.-H.; Heinz, T. F.; Reichman, D. R.; Muller, D. A.; Hone, J. C. *Nat. Mater.* **2013**, *12*, 554–561.

[30] Splendiani, A.; Sun, L.; Zhang, Y.; Li, T.; Kim, J.; Chim, C.-Y.; Galli, G.; Wang, F. *Nano Lett.* **2010**, *10*, 1271–1275.

[31] Mak, K.; Lee, C.; Hone, J.; Shan, J.; Heinz, T. *Phys. Rev. Lett.* **2010**, *105*, 136805.

[32] Chernikov, A.; Berkelbach, T. C.; Hill, H. M.; Rigosi, A.; Li, Y.; Aslan, O. B.; Reichman, D. R.; Hybertsen, M. S.; Heinz, T. F. *Phys. Rev. Lett.* **2014**, *113*, 076802.

[33] Dhakal, K. P. et al. *Nanoscale* **2014**, *6*, 13028–13035.

[34] Mak, K. F.; He, K.; Lee, C.; Lee, G. H.; Hone, J.; Heinz, T. F.; Shan, J. *Nat. Mat.* **2013**, *12*.

[35] Xu, X.; Yao, W.; Xiao, D.; Heinz, T. F. *Nat. Phys.* **2014**, *10*, 343–350.

[36] Novoselov, K. S.; Castro Neto, A. H. *Physica Scripta* **2012**, *T146*, 014006.

[37] Novoselov, K. S.; Geim, A. K.; Morozov, S. V.; Jiang, D.; Zhang, Y.; Dubonos, S. V.; Grigorieva, I. V.; Firsov, A. A. *Science* **2004**, *306*, 666–9.

[38] Liu, H. F.; Wong, S. L.; Chi, D. Z. *Chem. Vap. Dep.* **2015**, *21*, 241–259.

[39] Radisavljevic, B.; Radenovic, A.; Brivio, J.; Giacometti, V.; Kis, A. *Nat. Nano.* **2011**, *6*, 147–50.

[40] Wang, Q. H.; Kalantar-Zadeh, K.; Kis, A.; Coleman, J. N.; Strano, M. S. *Nat. Nanotech.* **2012**, *7*, 699–712.

[41] Cao, Y.; Liu, S.; Shen, Q.; Yan, K.; Li, P.; Xu, J.; Yu, D.; Steigerwald, M. L.; Nuckolls, C.; Liu, Z.; Guo, X. *Adv. Funct. Mater.* **2009**, *19*, 2743–2748.

[42] Kang, S. J.; Lee, G.-H.; Yu, Y.-J.; Zhao, Y.; Kim, B.; Watanabe, K.; Taniguchi, T.; Hone, J.; Kim, P.; Nuckolls, C. *Adv. Funct. Mat.* **2014**, *24*, 5157–5163.

[43] Xia, F.; Wang, H.; Xiao, D.; Dubey, M.; Ramasubramaniam, A. *Nat. Photon.* **2014**, *8*, 899–907.

[44] Perkins, F. K.; Friedman, A. L.; Cobas, E.; Campbell, P. M.; Jernigan, G. G.; Jonker, B. T. *Nano Lett.* **2013**, *13*, 668–73.

[45] Schedin, F.; Geim, A. K.; Morozov, S. V.; Hill, E. W.; Blake, P.; Katsnelson, M. I.; Novoselov, K. S. *Nat. Mater.* **2007**, *6*, 652–655.

[46] Voiry, D.; Yamaguchi, H.; Li, J.; Silva, R.; Alves, D. C. B.; Fujita, T.; Chen, M.; Asefa, T.; Shenoy, V. B.; Eda, G.; Chhowalla, M. *Nat. Mater.* **2013**, *12*, 850–5.

[47] Wang, Y. et al. *Nano. Lett.* **2015**, *15*, 4013–8.

[48] Chhowalla, M.; Shin, H. S.; Eda, G.; Li, L.-J.; Loh, K. P.; Zhang, H. *Nat. Chem.* **2013**, *5*, 263–75.

[49] Saito, Y.; Nakamura, Y.; Bahramy, M. S.; Kohama, Y.; Ye, J.; Kasahara, Y.; Nakagawa, Y.; Onga, M.; Tokunaga, M.; Nojima, T.; Yanase, Y.; Iwasa, Y. *Nat. Phys.* **2015**, *12*, 144–149.

[50] Costanzo, D.; Jo, S.; Berger, H.; Morpurgo, A. F. *Nat. Nanotech.* **2016**, *11*, 339–344.

[51] Lu, J. M.; Zheliuk, O.; Leermakers, I.; Yuan, N. F. Q.; Zeitler, U.; Law, K. T.; Ye, J. T. *Science* **2015**, *350*.

[52] Lee, B.; Chen, Y.; Fu, D.; Yi, H. T.; Czelen, K.; Najafov, H.; Podzorov, V. *Nat. Mat.* **2013**, *12*, 1125–9.

[53] Xie, W.; Liu, F.; Shi, S.; Ruden, P. P.; Frisbie, C. D. *Adv. Mat.* **2014**, *26*, 2527–32.

[54] Xie, W.; Wang, S.; Zhang, X.; Leighton, C.; Frisbie, C. D. *Phys. Rev. Lett.* **2014**, *113*, 246602.

[55] Xia, Y.; Cho, J. H.; Lee, J.; Ruden, P. P.; Frisbie, C. D. *Adv. Mat.* **2009**, *21*, 2174–2179.

[56] Susan, M. A. B. H.; Kaneko, T.; Noda, A.; Watanabe, M. *J. Am. Chem. Soc.* **2005**, *127*, 4976–83.

[57] Lee, K. H.; Kang, M. S.; Zhang, S.; Gu, Y.; Lodge, T. P.; Frisbie, C. D. *Adv. Mat.* **2012**, *24*, 4457–62.

[58] Atallah, T. L.; Gustafsson, M. V.; Schmidt, E.; Frisbie, C. D.; Zhu, X.-Y. *J. Phys. Chem. Lett.* **2015**, *6*, 4840–4.

[59] Li, Z. Q.; Podzorov, V.; Sai, N.; Martin, M. C.; Gershenson, M. E.; Di Ventra, M.; Basov, D. N. *Phys. Rev. Lett.* **2007**, *99*, 016403.

[60] Fischer, M.; Dressel, M.; Gompf, B.; Tripathi, A. K.; Pflaum, J. *Appl. Phys. Lett.* **2006**, *89*, 182103.

[61] Uchida, R.; Yada, H.; Makino, M.; Matsui, Y.; Miwa, K.; Uemura, T.; Takeya, J.; Okamoto, H. *Appl. Phys .Lett.* **2013**, *102*, 093301.

[62] Tsui, D.; Allen, S.; Logan, R.; Kamgar, A.; Coppersmith, S. *Surf. Sci.* **1978**, *73*, 419–433.

[63] Hulea, I. N.; Fratini, S.; Xie, H.; Mulder, C. L.; Iossad, N. N.; Rastelli, G.; Ciuchi, S.; Morpurgo, A. F. *Nat. Mat.* **2006**, *5*, 982–6.

[64] Gershenson, M. E.; Podzorov, V.; Morpurgo, A. F. *Rev. Modern Phys.* **2006**, *78*, 973–989.

[65] Bisri, S. Z.; Takenobu, T.; Takahashi, T.; Iwasa, Y. *Appl. Phys. Lett.* **2010**, *96*, 183304.

[66] Takenobu, T.; Takahashi, T.; Takeya, J.; Iwasa, Y. *Appl. Phys. Lett.* **2007**, *90*, 013507.

[67] Ullah, A. R.; Micolich, A. P.; Cochrane, J. W.; Hamilton, A. R. In *Microelectronics, MEMS, and Nanotechnology*; Tan, H. H., Chiao, J.-C., Faraone, L., Jagadish, C., Williams, J., Wilson, A. R., Eds.; International Society for Optics and Photonics, 2007; pp 680005–8.

[68] Yokota, Y.; Hara, H.; Harada, T.; Imanishi, A.; Uemura, T.; Takeya, J.; Fukui, K.-i. *Chem. Comm.* **2013**, *49*, 10596–8.

[69] Santosh, K. C.; Longo, R. C.; Addou, R.; Wallace, R. M.; Cho, K. *Nanotech.* **2014**, *25*, 375703.

[70] Zhou, W.; Zou, X.; Najmaei, S.; Liu, Z.; Shi, Y.; Kong, J.; Lou, J.; Ajayan, P. M.; Yakobson, B. I.; Idrobo, J.-C. *Nano Lett.* **2013**, *13*, 2615–2622.

[71] Vancsó, P.; Magda, G. Z.; Petö, J.; Noh, J.-Y.; Kim, Y.-S.; Hwang, C.; Biró, L. P.; Tapasztó, L. *Sci. Rep.* **2016**, *6*, 29726.

[72] Amani, M. et al. *Science* **2015**, *350*, 1065–8.

[73] Nan, H.; Wang, Z.; Wang, W.; Liang, Z.; Lu, Y.; Chen, Q.; He, D.; Tan, P.; Miao, F.; Wang, X. *ACS Nano* **2014**, *8*, 5738–5745.

[74] Berkelbach, T. C.; Hybertsen, M. S.; Reichman, D. R. *Phys. Rev. B* **2013**, *88*, 45318.

[75] Komsa, H.-P.; Krasheninnikov, A. V. *Phys. Rev. B* **2015**, *91*, 125304.

[76] Zhu, W.; Low, T.; Perebeinos, V.; Bol, A. A.; Zhu, Y.; Yan, H.; Tersoff, J.; Avouris, P. *Nano Lett.* **2012**, *12*, 3431–3436.

[77] Lince, J. R.; Hilton, M. R.; Bommannavar, A. S. *Surf. Coat. Tech.* **1990**, *43-44*, 640–651.

[78] Zhao, B.; Shang, C.; Qi, N.; Chen, Z.; Chen, Z. *Appl. Surf. Sci.* **2017**, *412*, 385–393.

[79] Fleischauer, P. D.; Lince, J. R. *Trib. Internat.* **1999**, *32*, 627–636.

[80] Cadiz, F. et al. *arXiv* **2017**,

[81] Cui, X. et al. *Nat. Nanotech.* **2015**, *10*, 534–540.

[82] Ajayi, O.; Ardelean, J.; Shepard, G.; Wang, J.; Antony, A.; Taniguchi, T.; Watanabe, K.; Heinz, T.; Strauf, S.; Zhu, X.-Y.; Hone, J. C. *2D Mat.* **2017**,

[83] Amani, M.; Addou, R.; Ahn, G. H.; Kiriya, D.; Taheri, P.; Lien, D.-H.; Ager, J. W.; Wallace, R. M.; Javey, A. *Nano Lett.* **2016**, *16*, 2786–2791.

[84] Li, G.; Zhang, D.; Qiao, Q.; Yu, Y.; Peterson, D.; Zafar, A.; Kumar, R.; Curtarolo, S.; Hunte, F.; Shannon, S.; Zhu, Y.; Yang, W.; Cao, L. *J. Am. Chem. Soc.* **2016**, *138*.

[85] Atallah, T. L.; Wang, J.; Bosch, M.; Seo, D.; Burke, R. A.; Moneer, O.; Zhu, J.; Theibault, M.; Brus, L. E.; Hone, J.; Zhu, X.-Y. *J. Phys. Chem. Lett.* **2017**, in press.

[86] Desai, S. B.; Madhvapathy, S. R.; Sachid, A. B.; Llinas, J. P.; Wang, Q.; Ahn, G. H.; Pitner, G.; Kim, M. J.; Bokor, J.; Hu, C.; Wong, H.-S. P.; Javey, A. *Science* **2016**, *354*.

[87] Liu, X.; Galfsky, T.; Sun, Z.; Xia, F.; Lin, E.-c.; Lee, Y.-H.; Kéna-Cohen, S.; Menon, V. M. *Nat. Photon.* **2015**, *9*, 30–34.

[88] Zhang, Y. J.; Oka, T.; Suzuki, R.; Ye, J. T.; Iwasa, Y. *Science* **2014**, *344*.

[89] Guo, Y.; Wei, X.; Shu, J.; Liu, B.; Yin, J.; Guan, C.; Han, Y.; Gao, S.; Chen, Q. *Appl. Phys. Lett.* **2015**, *106*, 103109.

[90] Tongay, S.; Suh, J.; Ataca, C.; Fan, W.; Luce, A.; Kang, J. S.; Liu, J.; Ko, C.; Raghunathanan, R.; Zhou, J.; Ogletree, F.; Li, J.; Grossman, J. C.; Wu, J. *Sci. Rep.* **2013**, *3*, 2657.

[91] Wang, H.; Zhang, C.; Rana, F. *Nano Lett.* **2015**, *15*, 339–345.

[92] McDonnell, S.; Addou, R.; Buie, C.; Wallace, R. M.; Hinkle, C. L. *ACS Nano* **2014**, *8*, 2880–2888.

[93] Han, H.-V.; Lu, A.-Y.; Lu, L.-S.; Huang, J.-K.; Li, H.; Hsu, C.-L.; Lin, Y.-C.; Chiu, M.-H.; Suenaga, K.; Chu, C.-W.; Kuo, H.-C.; Chang, W.-H.; Li, L.-J.; Shi, Y. *ACS Nano* **2016**, *10*, 1454–1461.

[94] Liu, B.; Zhao, W.; Ding, Z.; Verzhbitskiy, I.; Li, L.; Lu, J.; Chen, J.; Eda, G.; Loh, K. P. *Adv. Mat.* **2016**, *28*, 6457–6464.

[95] Lee, G.-H.; Cui, X.; Kim, Y. D.; Arefe, G.; Zhang, X.; Lee, C.-H.; Ye, F.; Watanabe, K.; Taniguchi, T.; Kim, P.; Hone, J. *ACS Nano* **2015**, *9*, 7019–7026.

[96] Jeong, J.; Aetukuri, N.; Graf, T.; Schladt, T. D.; Samant, M. G.; Parkin, S. S. P. *Science* **2013**, *339*.

[97] Lin, Y.; Ling, X.; Yu, L.; Huang, S.; Hsu, A. L.; Lee, Y.-H.; Kong, J.; Dressel-haus, M. S.; Palacios, T. *Nano Lett.* **2014**, *14*, 5569–76.

[98] Krivosheeva, A. V.; Shaposhnikov, V. L.; Borisenko, V. E.; Lazzari, J.-L.; Waileong, C.; Gusakova, J.; Tay, B. K. *J. Semicond.* **2015**, *36*, 122002.

[99] Le, D.; Rawal, T. B.; Rahman, T. S. *J. Phys. Chem. C* **2014**, *118*, 5346–5351.

[100] Yin, Y.; Han, J.; Zhang, Y.; Zhang, X.; Xu, P.; Yuan, Q.; Samad, L.; Wang, X.; Wang, Y.; Zhang, Z.; Zhang, P.; Cao, X.; Song, B.; Jin, S. *J. Am. Chem. Soc.* **2016**, *138*, 7965–7972.

Appendix: My Publications

Publications Related to Doctoral Thesis

- Atallah, T. L.; Wang, J.; Bosch, M.; Seo, D.; Burke, R. A.; Moneer, O.; Zhu, J.; Theibault, M.; Brus, L. E.; Hone, J.; Zhu, X.-Y. Electrostatic Screening of Charged Defects in Monolayer MoS_2. *J. Phys. Chem. Lett.* **2017**, *8*, 2148-2152.

- Atallah, T. L.; Gustafsson, M. V; Schmidt, E.; Frisbie, C. D.; Zhu, X.-Y. Charge Saturation and Intrinsic Doping in Electrolyte-Gated Organic Semiconductors. *J. Phys. Chem. Lett.* **2015**, *6*, 4840-4844.

Other Publications

- Morris, J. D.; Atallah, T. L.; Park, H.; Ooi, Z.; Dodabalapur, A.; Zhu, X.-Y. Quantifying Space Charge Accumulation in Organic Bulk Heterojunctions by Nonlinear Optical Microscopy. *Org. Electron.* **2013**, *14*, 3014-3018.

- Morris, J. D.; Atallah, T. L.; Lombardo, C. J.; Park, H.; Dodabalapur, A.; Zhu, X.-Y. Mapping Electric Field Distributions in Biased Organic Bulk Heterojunctions under Illumination by Nonlinear Optical Microscopy. *Appl. Phys. Lett.* **2013**, *102*, 33301.

- Atallah, T. L.; Blankespoor, R. L.; Homan, P.; Hulderman, C.; Samas, B. M.; Van Allsburg, K.; Vrieze, D. C. Substituent Effects on the Amination of Racemic Allyl Carbonates Using Commercially Available Chiral Rhodium Catalysts. *Tetrahedron Lett.* **2013**, *54*, 5795-5798.

- Haan, S. L.; Smith, Z. S.; Shomsky, K. N.; Plantinga, P. W.; Atallah, T. L. Anticorrelated Electrons from High-Intensity Nonsequential Double Ionization of Atoms. *Phys. Rev. A* **2010**, *81*, 23409.

Submitted Publications

- Miyata, K.; Atallah, T. L.; Zhu, X.-Y. Lead Halide Perovskites: Crystal-Liquid Duality, Phonon Glass Electron Crystals, and Large Polaron Formation. *Sci. Adv.* [*under review*].

- Evans, T. J. S.; Schlaus, A.; Fu, Y.; Zhong, X.; Atallah, T. L.; Spencer, M .S.; Brus, L. E.; Jin, S.; Zhu, X.-Y. Continuous-Wave Polariton Lasing in Cesium Lead Bromide Perovskite Nanowires. *Sci. Adv.* [*under review*].

- O 'brien, E. S.; Trinh, M. T.; Kann, R. L.; Chen, J.; Elbaz, G. A.; Masurkar, A.; Atallah, T. L.; Paley, M. V; Patel, N.; Paley, D. W.; Kymissis, I.; Crowther, A. C.; Millis, A. J.; Reichman, D. R.; Zhu, X.; Roy, X. Single-Crystal-to-Single-Crystal Intercalation of a Low-Bandgap Superatomic Crystal. *Nat. Chem.* **2017** [*in press*].